Imaging the Urinary Tract: Fundamentals of Ultrasound, Computed Tomography, and Magnetic Resonance Imaging

John Hines, Jay A. Karajgikar, Joseph D. Giardina, and Barak Friedman

Principles of Ultrasound

Ultrasound is a type of mechanical energy that produces vibrations as it traverses any given medium. These vibrations create varying areas of pressure. The alternations between areas of high and low pressure are measurable against time and termed the *wave frequency* with Hertz used as the unit of measurement. By convention, it is generally accepted that the speed of sound propagation is 1540 m/s, which represents the average speed at which sound travels in soft tissues. The unit of time of a cycle of the wave is called the *period*, and the distance between wave crests is termed *wavelength* [1–3].

Ultrasound in Tissue

In order to compose an ultrasound image, pulses of sound are sent into the target tissue. These pulses are very short, approximately 1 ms or less, and as they move through tissue, echo signals are produced and reflected back toward the source, termed a *transducer*. Different tissues interact differently with these sound waves. They are reflected, refracted, and/or absorbed by the tissue structures and then captured by the transducer, which then formulates an image. It is these differences in tissue interaction, the *echotexture*, that allow for anatomical imaging to be formulated. Structures that

appear bright are termed *hyperechoic*, while structures that are dark are referred to as *hypoechoic* [1–3].

The amplitude of the echo signal of imaged tissues is dependent on the number of scatterers per unit volume, the acoustic impedance, the sizes of the scatterers, and the ultrasonic frequency. The term *hyperechoic* refers to tissue which yields higher scatter amplitude, and hypoechoic refers to tissue with lower scatter amplitude. Thus both are used to describe the scatter characteristics of tissue relative to the average background signal. Areas that appear hyperechoic are generally composed of greater numbers of scatterers and possess larger acoustic impedance differences as well as overall larger-sized scatterers. Acoustic scattering from nonspecular (diffuse) reflectors increases with frequency. Specular reflectors are largely independent of frequency. It is therefore usually possible to enhance the scattered echo signals by using higher ultrasound frequencies [1–3]:

Bright (hyperechoic): renal sinus fat and renal calculi
Dark (hypoechoic): renal pyramids
Uniform, midlevel echogenicity: renal cortex
Notable reflective surfaces: anterior surface of the kidney [3].

Smooth surfaces of tissue reflect sound waves in a rather predictable way, and when the angle of reflection is perpendicular to the tissue surface, a large proportion of the sound is reflected back to the transducer. This angle of reflection, termed the angle of incidence, is a key component of ultrasound imaging. When sound waves reflect off an irregular surface, a smaller proportion of the waves are reflected back to the transducer and often the strength of these waves is diminished. Thus these surfaces are termed diffuse (nonspecular) reflectors [1, 3, 4].

Impedance

Impedance is another factor in determining the strength of sound reflected by tissue surfaces or echoes. It describes differences in tissue density (denser and stiffer tissues having

J. Hines, MD (✉) • J.A. Karajgikar, MD • B. Friedman, MD
Department of Radiology, Hofstra North Shore LIJ
School of Medicine, New Hyde Park, NY 11040, USA
e-mail: Jhines@nshs.edu; jaykarajgikar@nshs.edu;
BFriedma@nshs.edu

J.D. Giardina, MD
Vascular Interventional Radiology, Mallinckrodt Institute
of Radiology, Washington University in St.
Louis School of Medicine, St. Louis, Missouri, USA
e-mail: giar55@gmail.com

greater impedance compared with those less dense tissues) and how sound is reflected differently at tissue interfaces. For example, the lung is much less dense than the liver, and thus, the liver has a higher impedance to sound waves than the lung. Sound is reflected differently at different tissue interfaces, and the sound that is not reflected is transmitted or absorbed. The echo strength is dependent on the amount of reflection and thus dependent on tissue interfaces with regard to their differences in impedance. Soft tissue adjacent to air-filled lungs provides a large difference in acoustic impedance. The sound waves incident on the soft tissue of the lungs are almost entirely reflected and appear very hyperechoic. In fact, so much of the beam is reflected that structures posterior to the air are not visualized. When adjacent tissues have similar acoustic impedances, only minor reflections of the incident energy will occur. Acoustic impedance gives rise to differences in transmission and reflection of ultrasound energy, which provides the foundation of pulse echo imaging [1, 3, 4].

Impedance values of biological tissue (unit=Z (rayl)):

Air-muscle—0.98
Fat-muscle—0.015
Liver-muscle—0.0003
Bone-muscle—0.41
Liver-kidney—0.00003 [3, 4]

Refraction

Similar to the behavior of waves of light energy, sound is refracted when it enters an interface at an angle which is non-perpendicular and when the densities of the mediums on both sides of the interface differ. The latter alters the speed at which the wave propagates and helps to create a change in the angle of propagation of the sound wave, termed the *refraction angle*. This angle increases with greater differences in tissue density and yields larger differences in the wave's speed as it travels through the two mediums. Refraction at interfaces between different tissues thus bends the sound wave beam and its reflected echoes. This is seen routinely at soft tissue-fluid as well as fat-muscle interfaces. A clinical example is demonstrated as *edge* (*refraction*) *artifact* encountered in the imaging of a simple cyst which demonstrates posterior acoustic enhancement with shadowing at the lateral edges (Fig. 2.1) [2–5].

Attenuation

Attenuation refers to decreases in sound beam strength as it travels through tissue. Frequency is a determining factor of attenuation, and the higher the frequency of the sound wave, the greater the attenuation. The penetrating power of sound is therefore limited at higher frequencies. Tissue density is another determining factor of attenuation. Reflections and
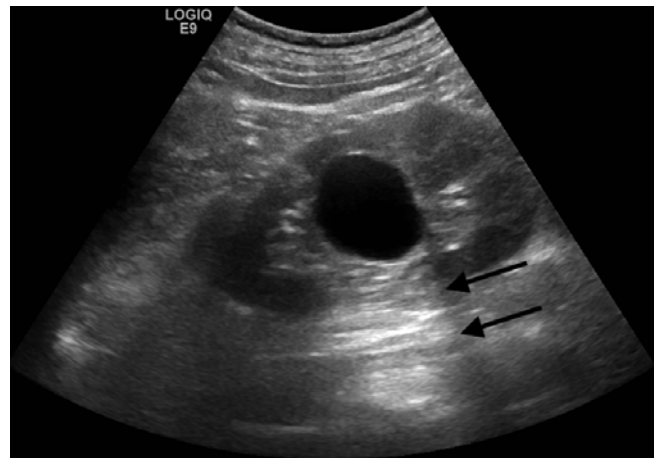

Fig. 2.1 Renal cyst. Sagittal sonographic image of the left kidney demonstrates a well-circumscribed, anechoic, thinly walled lesion with posterior acoustic enhancement (*black arrows*), a finding which is often used to definitively characterize a lesion as cystic. At the lateral edges of the enhanced echoes, there is a faint shadow representing *edge* (*refraction artifact*) which results from bending of the sound wave from its expected path
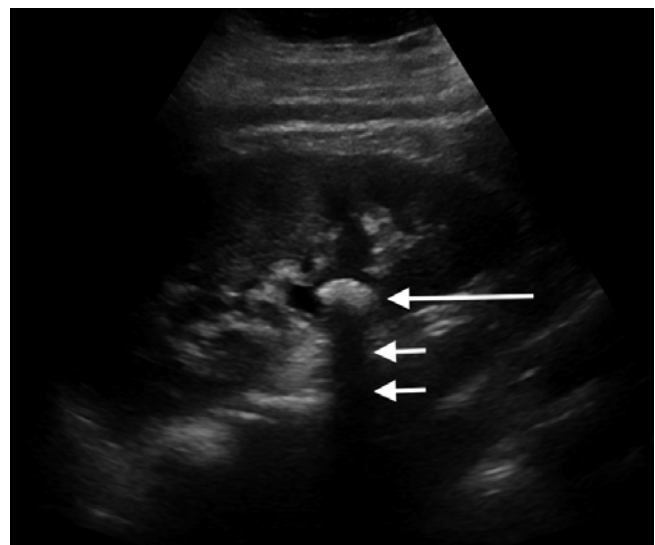

Fig. 2.2 Renal calculus. Sagittal sonographic image of the right kidney demonstrates a calcified renal stone (*large white arrow*) with the classic appearance of an echogenic lesion causing posterior acoustic shadowing (*small white arrows*)

refractions are some of the reasons for this phenomenon. Another is the conversion of the sound energy to heat.

Acoustic shadowing is an example of attenuation differences in action. The term refers to lost through transmission of the sound beam. An example is seen in renal calculi which both absorb and reflect the sound beam, resulting in acoustic shadows posterior to the calculus, due to marked attenuation of the sound beam (Fig. 2.2). In contrast, posterior acoustic enhancement is a phenomenon produced when attenuation of a structure is less than that of surrounding tissue, resulting in greater amplitude of the beam posterior to the structure.

This is falsely displayed as an increase in echogenicity of the tissue posterior to the weakly attenuating structure. In clinical practice, this is commonly seen in the setting of a simple renal cyst (Fig. 2.1) or any other fluid-containing structure, such as the urinary bladder [2–5]:

Attenuation coefficients for selected tissues at 1 MHz
Material attenuation coefficient (dB/cm)
Water 0.0002
Soft tissue 0.3–0.8
Fat 0.5–1.8
Bone 13–26
Air 40 [4]

Pulse-Echo Imaging Modes

Amplitude Mode (A-Mode)

A-mode is no longer utilized in the clinical setting. A short ultrasound pulse propagates into tissue and creates an echo, and this echo is received, amplified, and displayed as amplitude vs. distance [2, 3, 5].

Motion Mode (M-Mode)

Echo signal amplitudes are modulated according to levels of brightness and are displayed in a variety of shades of gray. The ultrasound beam is fixed at one position yet is observed in real time while scanning, allowing for the imaging of the motion of moving structures. A clinical example of M-mode use is in echocardiography, in which real-time evaluation of myocardial motion is performed [2, 3, 5].

Brightness Mode (B-Mode)

This mode produces a 2D image via modulating the echo signal amplitudes to various levels of brightness. This allows echoes to be displayed as lines with the imaged composed of "point-by-point variations in brightness level aka various shades of gray." In practice, structures that are more sound wave reflective appear more hyperechoic than those that are less reflective. Furthermore, the pulse line can be swept across tissue planes and produce cross-sectional imaging in the 2D plane [2, 3, 5].

Transducers

The sound beam is created by the transducer which makes use of a phenomenon called the piezoelectric effect to convert electrical energy into vibrational energy. This is accom-plished by alternating electric current to the transducers crystal which causes expansion and contraction. Thus this produces vibrations and therefore sound waves. In addition to producing the sound beam, the transducer is also capable of receiving the reflected sound waves, referred to as echoes. Upon receipt, the crystal vibrates at the received echoes' frequency and converts that frequency into electrical current which is processed and converted into the ultrasound image [2, 3, 5].

Array technology allows for electronic focusing to a variety of depths with multiple focal zones from the same transducer. These capabilities yield better image quality/resolution/sharpness. Older transducers, in contrast, generated the sound beam with one element, causing the beam to converge at a focal zone, proximal to which was termed the *near field* and distal to which was termed the *far field*, where the sound waves diverged. The depth of the focal zone was determined by the characteristics of this single element [2, 3, 5].

Linear Array

Linear array transducers are composed of parallel scan lines which are perpendicular to the surface of the transducer. These utilize higher frequencies and provide high-resolution imaging of fascial planes that lay parallel to the skin surface. Linear arrays are most commonly used for imaging superficial and small parts and for musculoskeletal and vascular imaging where there is a need for highly detailed images [3, 5].

Curvilinear Array

These transducers are composed of crystals aligned in a convex arrangement, and thus, the scan lines diverge as the sound beam travels deeper into the scanned tissue. They typically utilize lower frequencies, allowing for deeper tissue penetration compared to linear high-frequency imaging. Interpolation is often required to fill in the gaps in the image produced by the diverging sound waves. The advantage of the curved array is that it produces a larger field of view for deeper tissue structures. It is often used for abdominal and obstetric imaging [3, 5].

Phased Array

These specialized transducers are composed of many more, often approximately 100, elements. They produce pulsed beams for each scan line, and thus, the beam can be steered in a different fashion than, for example, the linear array. The transducer also has a rather narrow face and the end result of

its image formation is one with a large lateral view of deeper tissue [3, 5].

A variety of modified transducer arrays are available for specialized imaging tasks by taking advantage of different focus strategies for specific anatomic regions. For example, endorectal probes are utilized for transrectal prostate biopsy, and endoesophageal probes are utilized for transesophageal echocardiography.

Types of Transducer Probes

Endorectal
Endoesophageal
Endovaginal
Endourethral
Endovascular [3, 5]

Image Resolution

Lateral Resolution

Lateral resolution refers to the minimum measurable separation of objects that lay parallel to the face of the transducer. Objects appear separated if their separation is in fact greater than the width of the sound beam. Higher-frequency transducers produce a longer near field, which is the narrowest portion of the beam. The near field is the region at which lateral resolution is the greatest. Higher-frequency transducers produce a narrow beam width, which decreases the amount of beam dispersion, which occurs in the far field. This thus allows for better lateral resolution [3, 5]. Focusing the beam further enhances lateral resolution by narrowing the beam width at a selected area of tissue.

Axial Resolution

Axial resolution refers to the minimum measurable separation of objects along the axis of the beam. The beam pulse length is the principal factor. A pulse length longer than twice the object separation will not generate resolvable echoes. Two basic techniques in which short pulses are generated are through broad bandwidth pulses and high-frequency beams. Therefore, broad bandwidth and high-frequency transducers are capable of producing short pulses and thus higher-resolution imaging [3, 5].

Elevational Resolution

Elevational resolution refers to slice thickness and is the same entity as lateral resolution but refers to the plane orthogonal to the image plane. The major contributing factor is beam width in this plane. Electronic control of transducers allows for other features that optimize image resolution. In modern ultrasound machines, the majority of these are automated upon selection of specific imaging protocols. These have the potential to improve image quality through the focus and filter of an echo upon its return to the transducer and help to enhance lateral resolution of the image by decreasing noise from the outer edges of the beam. Examples include:

Receive focus: received echoes from single pulse are electronically focused to account for location in the beam.
Dynamic aperture: aperture or sensitive area of the transducer is modified on reception to help eliminate side lobe or scattered signals from the edge of the beam.
Apodization: the sensitivity of individual transducer elements in an array is varied to help define the beam on transmit or reception [3, 5].

Transmit Power Control

The modulation of transmit power affects the pulse amplitude from the transducer. Stronger, greater amplitude pulses produce stronger returned echoes. This improves signal to noise ratio and increases the maximum depth of imaging. There is a potential risk of adverse bioeffects with prolonged exposure to high transmit power pulses in diagnostic ultrasonography; however, there are no reported confirmed cases. Nevertheless, "prudent and conservative" use of diagnostic sonography under the ALARA principle encourages the use of the lowest possible transmit power to produce diagnostic quality images [1, 5].

Frequency Selection

The ultrasound transducer has a broad frequency bandwidth which corresponds to the emitted pulse. The "nominal" frequency of a transducer is usually the center frequency of the bandwidth. As the frequency is increased, spatial resolution improves; however, the penetration of the beam decreases. Conversely, lower frequencies allow for greater penetration albeit with poorer spatial resolution. Thus the selection of transducer frequency is dependent on the clinical situation and requires a balance between the desired depth of penetration and spatial resolution [1, 5].

Doppler

Doppler ultrasound allows for clinical assessment of the presence or absence of flow within a vessel or tissue and can give information on blood flow direction, pulsatility,

and velocity. Doppler ultrasound processes frequencies of returning echoes from the imaged tissue to compose an image, as opposed to gray-scale sonography that utilizes the amplitude of the returning echoes. The foundation of Doppler ultrasound is the so-called Doppler effect. This refers to the change in frequency of a sound wave that occurs due to the relative motion of either the source, the observer (transducer), or the tissue medium. A commonly used example is the way in which the sound pitch of a moving train's whistle changes as it passes an observer. Clinically, blood cells act as moving reflectors of the ultrasound beam, and thus, blood flowing toward the transducer reflects the beam at a relatively higher frequency than blood flowing away [1, 6, 7]. The same transducers utilized for gray-scale imaging are capable of Doppler imaging. Three major Doppler imaging techniques are utilized clinically and discussed in the following sections.

Pulsed Wave (Spectral) Doppler

This is based on the velocity of a selected sample volume of blood flow and generates a waveform based upon directionality of flow: Flow toward the transducer is plotted above the baseline, and flow away from the transducer is plotted below. The velocity of the blood flow is demonstrated as the wave amplitude, and the characteristics of the waveform shape allow clinical inferences to be made about the type of flow. Spectral Doppler allows for the analysis of multiple different vessels at different depths and provides a high range of resolution and specificity due to the sampling component [1, 5, 7].

Color Doppler

This is a 2D depiction of blood flow which is superimposed on a gray-scale image of the tissue imaged. Relative direction of flow is depicted and based upon the average velocity of the blood. By convention, red typically is used for blood flowing toward the transducer and blue used for blood flowing away, although these settings can be easily switched. Color Doppler allows for the characterization of the quality of the blood flow, for example, turbulent vs. laminar flow. The intensity of the color display also varies as a depiction of the flow intensity (i.e., lighter shades depicting higher-frequency shifts). Objects that are stationary are depicted in gray scale only. Color Doppler therefore yields important clinical information about the overall flow to the imaged region and can help one choose where to place a spectral Doppler sampling window. The advantage of color Doppler is that it is a relatively easy technique for confirming the presence or absence of flow and visualizing small vessels, such as in the testes. Limitations include lower spatial resolution vs. gray-scale imaging as well as its relative insensitivity to slow flow or flow in small-caliber vessels for which spectral Doppler is superior [1, 5, 7].

Power Doppler

Power Doppler provides a display of the strength of the Doppler signal in contrast to the average shift of frequency. The color and shade displayed on the image are dependent upon the volume of the flowing blood. The primary advantage of power Doppler is a high sensitivity for detecting flowing blood. It is especially useful for the detection of slow flow or blood within very small vessels. Power Doppler is not susceptible to aliasing, in contrast to spectral and color Doppler. Unlike color and spectral Doppler, there is no reliance upon the Doppler angle, and thus, images of vessels in the perpendicular plane are possible to obtain. The disadvantages are that power Doppler does not provide any information about the directionality or velocity of blood flow. Power Doppler is vulnerable to motion, either of the transducer or of the tissue which manifests as an intense flash of color on the monitor, termed *flash artifact* [1, 5, 7].

Ultrasound Applications for the Genitourinary System

Normal Renal Anatomy

The normal ultrasound appearance of the kidneys is one of paired retroperitoneal structures. Each kidney is enclosed by a dense capsule, which itself is then surrounded by perinephric fat enclosed in Gerota's fascia. Sonographically, the kidney is conventionally imaged in the transverse and sagittal planes. Normal renal parenchyma in the longitudinal image is homogeneous with the normal cortex appearing more hyperechoic relative to the medulla. The medullary pyramids are thus hypoechoic in appearance relative to the cortex. They abut the renal sinus fat, which appears relatively hyperechoic. The center of the longitudinally displayed kidney is a complex of rather dense-appearing structures which include the peripelvic fat, renal vessels, lymphatic vessels, and normal collecting system. The normal vascular pedicle and the small intrarenal vasculature and renal perfusion are often well visualized and interrogated with the use of Doppler imaging to demonstrate the quality and quantity of flow [2, 8].

Renal Masses

Simple cysts (Fig. 2.1) are the most common benign adult renal mass, and ultrasound has proven an effective tool in evaluating renal cysts, allowing for differentiation from other cystic and solid renal masses. Simple cysts are commonly round, demonstrate a clearly defined thin wall, and lack internal echoes. The latter of these produce a characteristic feature known as *posterior acoustic enhancement*. The presence of internal septations, nodular components, internal echoes, and calcifications are more worrisome features.
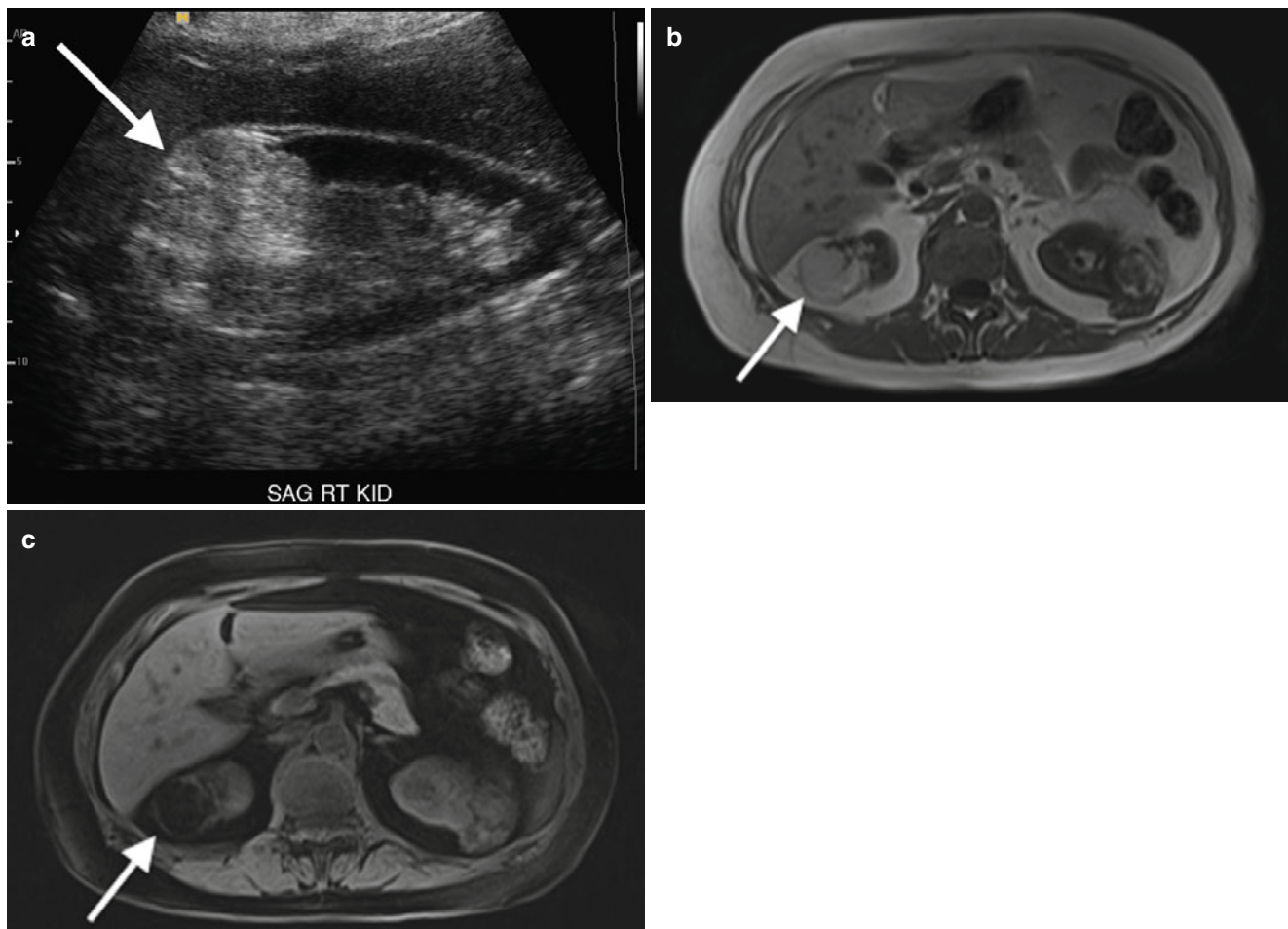
Fig. 2.3 Renal angiomyolipoma. Sagittal gray-scale sonographic image of the right kidney (**a**) demonstrates a rounded, hyperechoic, and nonshadowing solid mass at the upper pole of the kidney (*arrow*), consistent with angiomyolipoma. Accompanying non-contrast axial T1 in-phase (**b**) and T1 fat-saturated images (**c**) demonstrate the same mass to have high signal on the T1-weighted image (**b**) and diffuse signal loss (**c**) on the fat-suppressed image, confirming the diagnosis

Complex or septated cystic renal masses as well as solid masses raise suspicion of neoplasm (vs. abscess or hematoma) [2, 9, 10].

Sonographic characteristics of solid lesions include delineation of the posterior wall, lack of through transmission, and internal echoes. In the past, color flow and Doppler imaging were utilized to help differentiate different types of solid renal neoplasms. Ultrasound characterization of solid renal masses is more limited compared to cystic lesions, and more advanced imaging modalities such as CT and MR are indicated for further evaluation [2].

Angiomyolipoma (Fig. 2.3) is a benign, fat-containing renal mass that has a characteristic sonographic appearance. Lipid-rich lesions will demonstrate a characteristic homogeneous hyperechoic appearance and allow for a presumptive diagnosis, although infrequently this appearance can overlap with renal cell carcinoma. Therefore, additional imaging with CT is necessary to confirm the presence of macroscopic fat [9, 10].

Ultrasound can offer useful evaluation of mass lesions of the renal collecting system. Commonly, calcified calculi (Fig. 2.2) demonstrate the classic appearance of an echogenic focus with *posterior acoustic shadowing*. Even poorly or noncalcified calculi tend to demonstrate a hyperechoic echotexture and often shadow. Other lesions such as hematoma and neoplasm are often distinguishable from calculi, but their definitive diagnosis is better obtained via urologic procedures or additional imaging [2].

Overall, sonography is limited in its ability to stage the extent of malignant disease, which is better accomplished with CT and/or MRI.

Renal Failure

Ultrasound is commonly employed in the evaluation of renal failure as obstructive uropathy is an easily identifiable cause. Hydronephrosis (Fig. 2.4) is the hallmark of renal failure
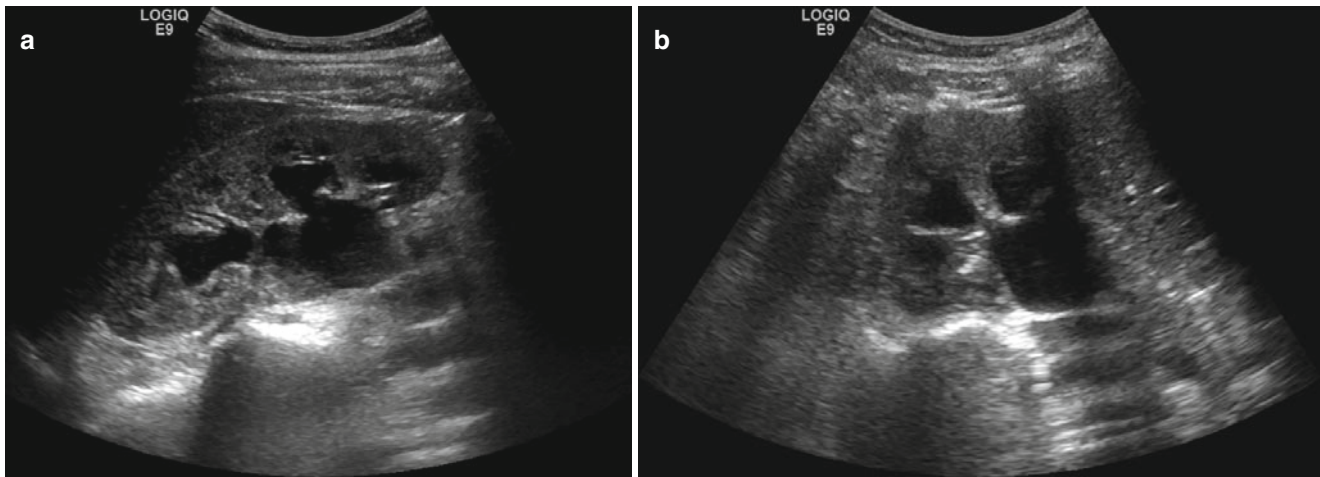
Fig. 2.4 Hydronephrosis. Sagittal (**a**) and transverse (**b**) sonographic images of the right kidney. The renal collecting system is symmetrically dilated, including dilatation of the renal calyces and central collecting system

due to obstruction and is characterized by the loss of the normally echogenic renal sinus which is replaced by a dilated hypoechoic collecting system. The level of dilatation of the calyces, infundibula, renal pelvis, and proximal ureter as well as the degree of parenchymal thinning can aid in inferring the degree and chronicity of the obstruction. Differential diagnostic considerations include parapelvic cysts, megacalyces, calyceal diverticula, and extrarenal pelvises. Post-intervention, ultrasound serves as an inexpensive and rapidly performed imaging study to assess for residual collecting system dilatation [2, 8].

Renal Transplant

The pelvic and superficial location of the transplanted kidney allows for it to be interrogated well by sonography. Postoperative perinephric collections, such as lymphoceles, urinomas, and hematomas, are usually identifiable. With decreased urine output, changes in renal volume and perfusion can be evaluated with sonography and allow for distinguishing obstruction from other transplant-related pathologies [2, 11].

Assessment of renal function is best accomplished with radionuclide imaging as the gray-scale ultrasound appearance in renal failure is rather nonspecific. Such findings include renal enlargement, increased cortical thickness, increased/decreased cortical echogenicity and loss of corticomedullary differentiation, prominent pyramids, thickness of the collecting system, and central sinus effacement. Ultrasound does however serve as an important tool in evaluating vascular complications of transplantation. Although conventional angiography remains the gold standard for the diagnosis of vascular complications, spectral and color Doppler ultrasound provide an excellent and noninvasive

assessment of affected vessels. Pathologies typically encountered include renal arterial or venous occlusion or stenosis and pseudoaneurysms and arteriovenous fistulae [11].

Renal artery stenosis (Fig. 2.5) is the most common vascular complication of transplantation, reported in up to 10 % of patients. Color Doppler interrogation of a stenotic segment will demonstrate areas of focal aliasing. These regions can then be selected for spectral Doppler evaluation to quantify the degree of stenosis, which can then be evaluated with duplex Doppler techniques to characterize and grade the abnormality. Spectral Doppler criteria for significant stenoses include (a) velocities greater than 2 m/s or focal frequency shift greater than 7.5 kHz (when a 3-MHz transducer is used), (b) a velocity gradient between stenotic and prestenotic segments of more than 2:1, and (c) marked distal turbulence (*spectral broadening*). The presence of the classically described "*tardus parvus*" ("late, small" in Latin) waveforms may further support the diagnosis; however, they are not always present. If there is no significant flow abnormality demonstrated, renal arterial stenosis can be excluded [10–12].

Urinary Bladder

The normal sonographic appearance of the urinary bladder is a globular, hypoechoic structure whose shape is variable, depending on the level of distension and the patient's position at the time of examination. The wall appears hyperechoic, smooth, and diffusely symmetric in thickness. When the normal bladder is distended, the lumen should be anechoic [2].

Bladder tumors can sometimes be visualized sonographically. Polypoid lesions (Fig. 2.6) appear as intraluminal soft tissue projections which are fixed to the bladder wall and are
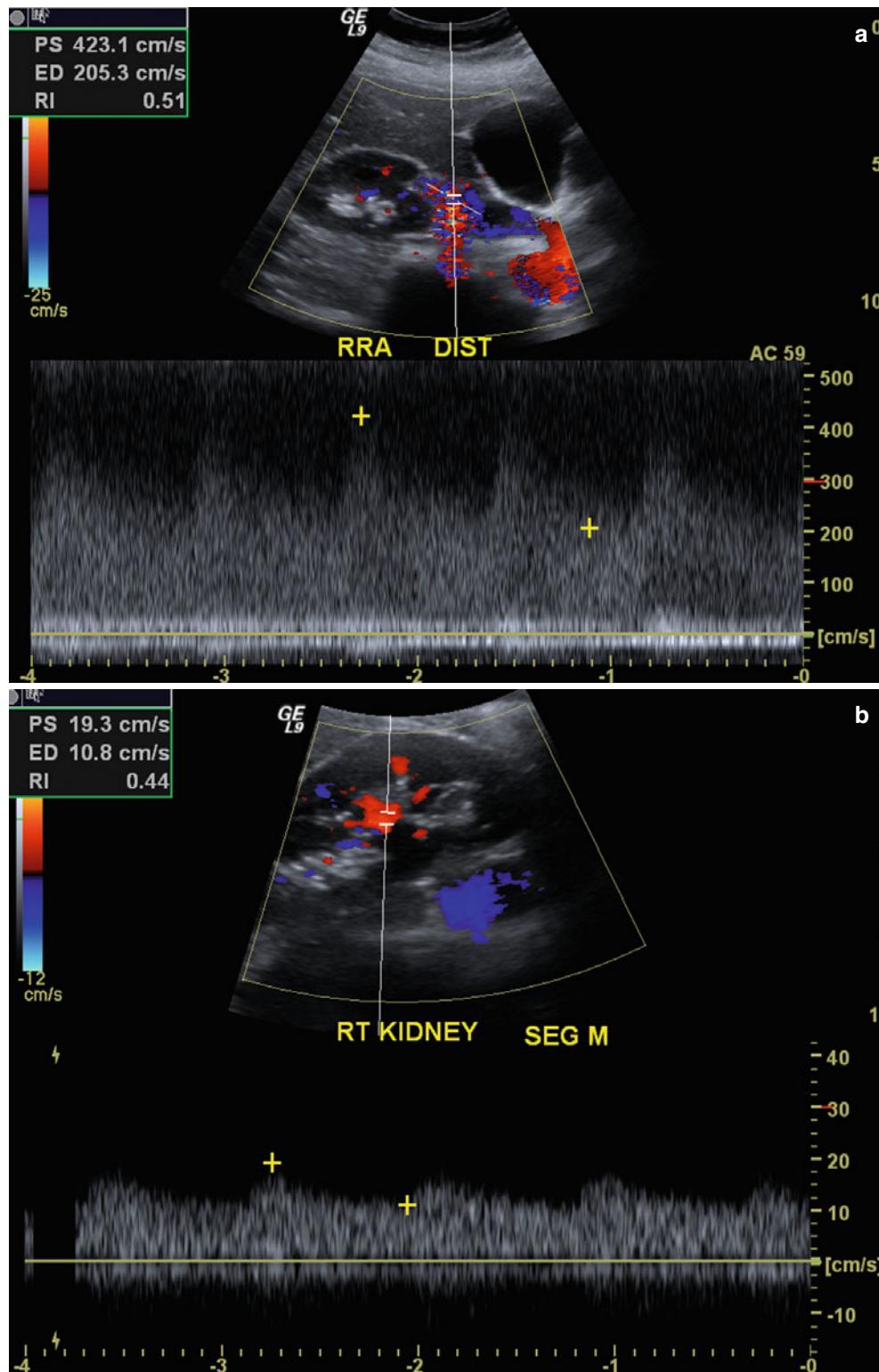
Fig. 2.5 Renal artery stenosis. Spectral Doppler sonographic images of the right renal artery, (**a**) at the level of a high-grade stenosis in the distal renal artery and (**b**) at the level of the segmental arteries, distal to the stenosis. (**a**, **b**) Abnormally high velocity is demonstrated at the level of the renal artery stenosis, while the arterial waveforms distal to the stenosis (**b**) show an abnormally delayed systolic upstroke with low amplitude ("tardus parvus") with corresponding low velocity. (**c**) Digitally subtracted image from renal arteriogram in the same patient shows a high grade mid-arterial stenosis (*arrow*). *Normal renal arterial waveform.* (**d**) A normal low-resistance waveform and velocity are demonstrated in the left renal artery in a different patient. Note the rapid systolic upstroke, with peak <150 cm/s and continuous low-resistance flow throughout diastole
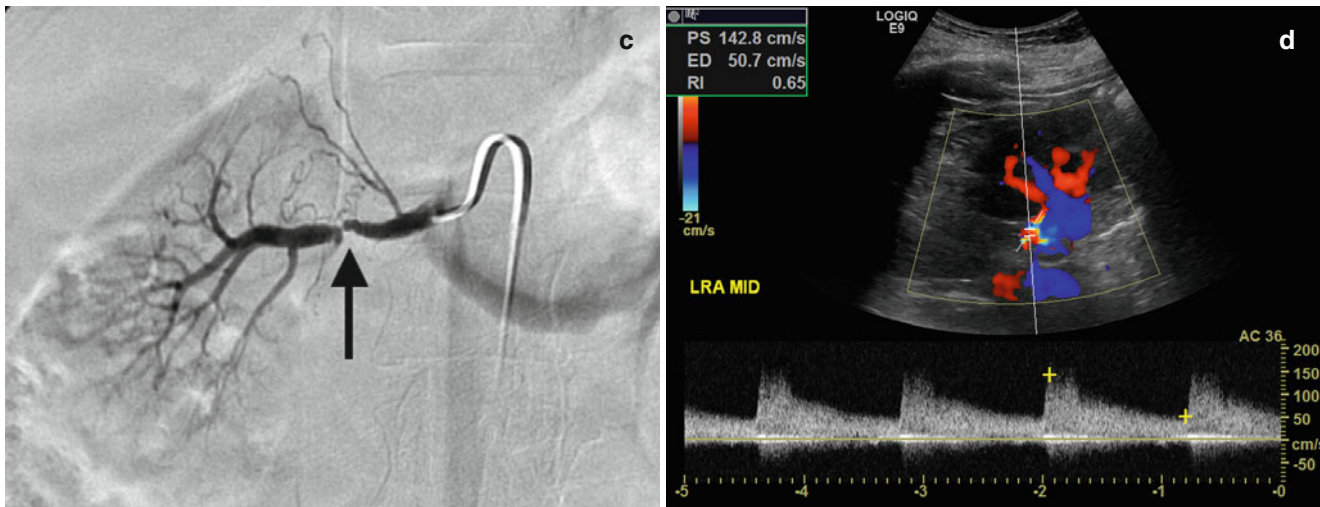
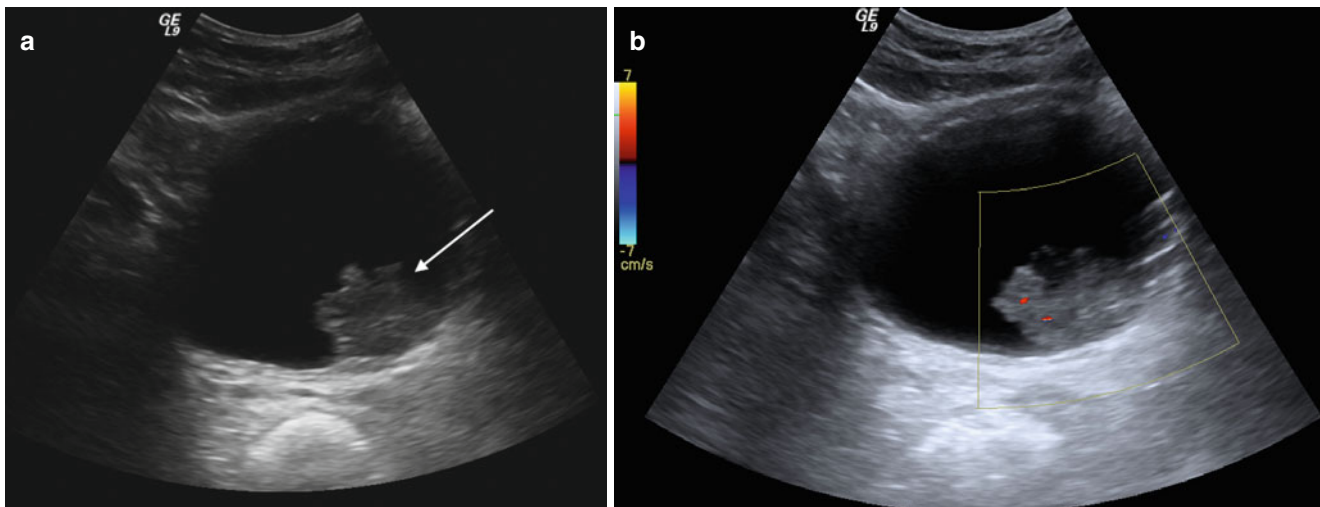**Fig. 2.5** (continued)

Fig. 2.6 Urinary bladder neoplasm. Transverse gray-scale (**a**) and color Doppler (**b**) sonographic images of the urinary bladder demonstrate a solid, exophytic mass within the urinary bladder lumen (*arrow* (**a**)) without any posterior acoustic shadowing and (**b**) with internal vascular color Doppler signal, indicative of a solid, vascularized lesion, rather than blood clot, adherent debris, or non-shadowing calculus

nonmobile with patient change in position, in contrast to mass-like lesions such as hematoma and calculi. Tumors are solid lesions in contrast to ureteroceles which, although they are also fixed to the bladder wall, have a distinct sonographic appearance with a thin echogenic wall and anechoic (cyst-like) center. Calculi within the bladder behave sonographically as in other areas of the GU tract with hyperechoic echotexture and posterior acoustic shadowing. Calculi will move as the patient changes position unless lodged at the ureterovesical junction [2].

Prostate

The normal sonographic appearance of the prostate is a symmetric triangular ellipsoid gland circumscribed by a fibrous capsule. The capsule itself appears as a continuous thin and hyperechoic layer of tissue. Internally the prostate demonstrates multiple fine diffuse homogeneous echoes which likely result from the interfaces of the myriad of small glands within. The posterior peripheral zone systolic velocity can typically be differentiated from the more anterior

peripheral zone, the central and transition zones, and the fibromuscular stroma [2].

Transrectal ultrasound has been shown to be useful in evaluating benign and malignant prostatic disease and plays a valuable role in biopsy and assessment of treatment of patients with prostate carcinoma (Fig. 2.7c). Note, however, that transrectal ultrasound is useful only to localize the prostate and not for the identification of lesions [2, 12–15].

Commonly used transrectal transducers used for prostate imaging range in frequency from 6.0 to 7.5 MHz. The higher frequency allows for detailed images; however, penetration of the beam is limited and thus the anterior prostate is often incompletely visualized. Most transducers are biplanar and provide images in the transverse and sagittal planes. The transverse plane allows for better visualization of the lateral margins, while the sagittal plane provides better images of the gland's apex and base [2, 12, 14, 15].

Currently, sonographic diagnostic evaluation of the prostate has a limited role in comparison with MRI (Fig. 2.7a, b). The anterior prostate is often insufficiently visualized, and
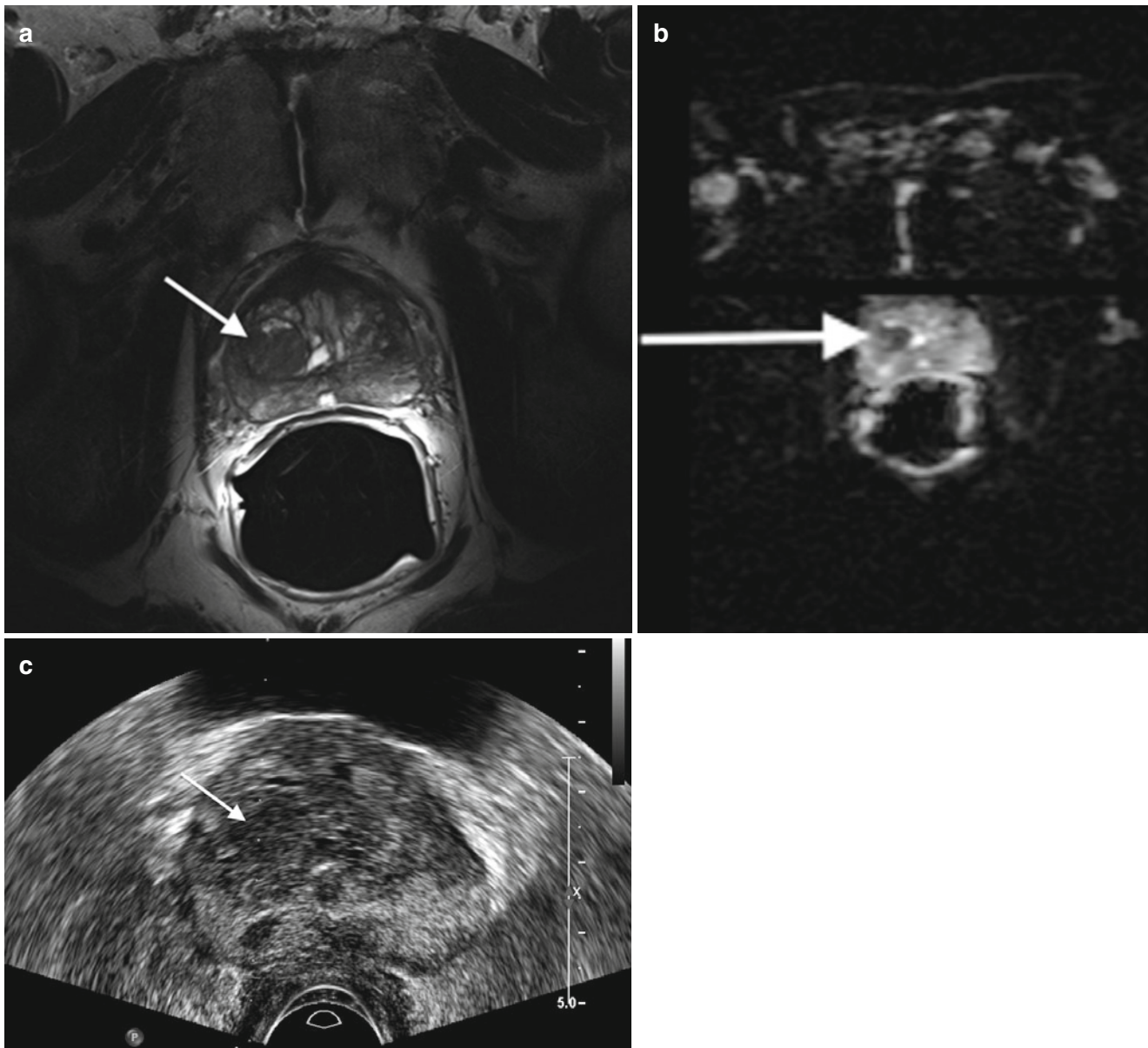
Fig. 2.7 Prostate carcinoma. (**a**) Axial T2- and (**b**) diffusion-weighted images of a right central prostate gland carcinoma (*arrows* (**a**, **b**)). (**c**) Transverse transrectal sonographic image of the prostate obtained during transrectal fusion biopsy demonstrates the lesion as a heterogeneous hypoechoic mass (*arrow*)

thus lesions in this region can go undetected. Additionally, many benign lesions as well as normal structures have similar sonographic appearances to small malignant lesions. Some carcinomas, in fact, are completely isoechoic and therefore the utility for diagnostic prostatic ultrasound is quite limited. It is becoming increasingly evident that supplementing the work-up of prostate cancer with prostate MRI when used in conjunction with transrectal ultrasound-guided biopsy will result in much higher yield for tissue diagnosis of malignancy [2, 12–15].

Penis

Sonographic evaluation of the penis is ideally conducted with a high-frequency linear transducer. This provides good visualization of the two corpora cavernosa, which are demonstrated as symmetric structures of homogenous mixed echogenicity which is due to the many interfaces of the vascular sinusoids. In contrast to the two corpus cavernosa, the corpus spongiosum normally appears mildly hypoechoic in comparison. The fibrous tunica albuginea appears as a hyperechoic line forming the intercavernous septum and provides a region of posterior acoustic shadowing between the corpora. Color and spectral Doppler sonography can evaluate penile vessel patency and characterize blood flow [2, 16].

Most applications of penile sonography occur in the acute setting. Acute conditions of the penis lend themselves to evaluation with ultrasound due to its wide availability and the real-time assessment it provides. Penile fracture results from tearing of the tunica albuginea leading to rupture of the corpora. Ultrasound is capable of demonstrating tears and the extent of the associated injury. The tear is visualized as a segmental discontinuity of the tunica albuginea, and associated hematoma may be visualized deep to the Buck fascia or subcutaneously. A secondary sign suggesting associated urethral injury is the presence of echogenic air in the cavernosa. The evaluation of the urethra with ultrasound is however limited, and when there is clinical concern of urethral injury, retrograde urethrography is indicated [2, 16].

Mondor disease of the penis, thrombophlebitis, or thrombosis occurs in the dorsal vein. Color Doppler evaluation serves in diagnosis and in monitoring patients. Sonographic findings include a lack of blood flow and noncompressibility of the dorsal vein, characteristic of thrombosis [2, 16].

Scrotal Ultrasound

The scrotum and its contents are superficial structures and thus well visualized with sonography. Scrotal pain and swelling prompt evaluation and sonography allows for differentiation between tumors, orchitis/epididymitis, torsion of the spermatic cord, and traumatic lesions such as fracture. Testicular and paratesticular malignant tumors are typically hypoechoic in appearance, and identification of such a mass demands surgical intervention in most scenarios. Nonseminomatous tumors can demonstrate increased vascular flow on Doppler imaging, while seminomas characteristically demonstrate homogeneous echotexture in contrast to embryonal tumors. Epididymitis is typically characterized by an enlarged and hypoechoic epididymis due to edema with hypervascularity on color Doppler imaging. Often, there is a reactive hydrocele accompanying the lesion. Epididymo-orchitis can have similar findings, as well as an enlarged and hypervascular testis [2, 17].

Clinically, distinguishing between testicular torsion (Fig. 2.8) and epididymo-orchitis can be difficult, and ultrasound has been found to be quite useful. In early torsion (approximately 1–3 h), echogenicity of the testes appears normal. As time goes on, there is enlargement of the torsed testis, and it will appear increasingly heterogeneous in echotexture. Evaluating the spermatic cord in suspected torsion is critical as a torsed cord can be visualized in the external inguinal orifice and aid in making the diagnosis. The intrascrotal portion of the torsed and edematous cord can appear as a rounded echogenic extratesticular mass. The orientation of the cord, testis, and epididymis can be inverted. The diagnosis is further strengthened with the evaluation of testicular blood flow, with the affected side demonstrating abnormal or absent flow compared to the normal testis. Comparative imaging with transverse views, including pulsed Doppler imaging can yield important information regarding decreased or reversed diastolic blood flow to the affected testis when compared to the normal side [17].

Traumatic injury to the scrotum lends itself to sonographic evaluation as the pain and swelling often limit physical examination. Findings include extratesticular hematoma and testicular rupture, the latter of which should be suspected in the case of poorly defined testicular margins and/or disruption of capsular blood flow. The echotexture of extratesticular/scrotal hematoma evolves over time with a more echogenic acute appearance transitioning to a more hypoechoic appearance in the subacute and later stages [17].

Varicocele

A varicocele (Fig. 2.9) will appear as a series of tortuous anechoic tubular structures either around, above, or below the testis. There is some variation in the caliber of the ves-
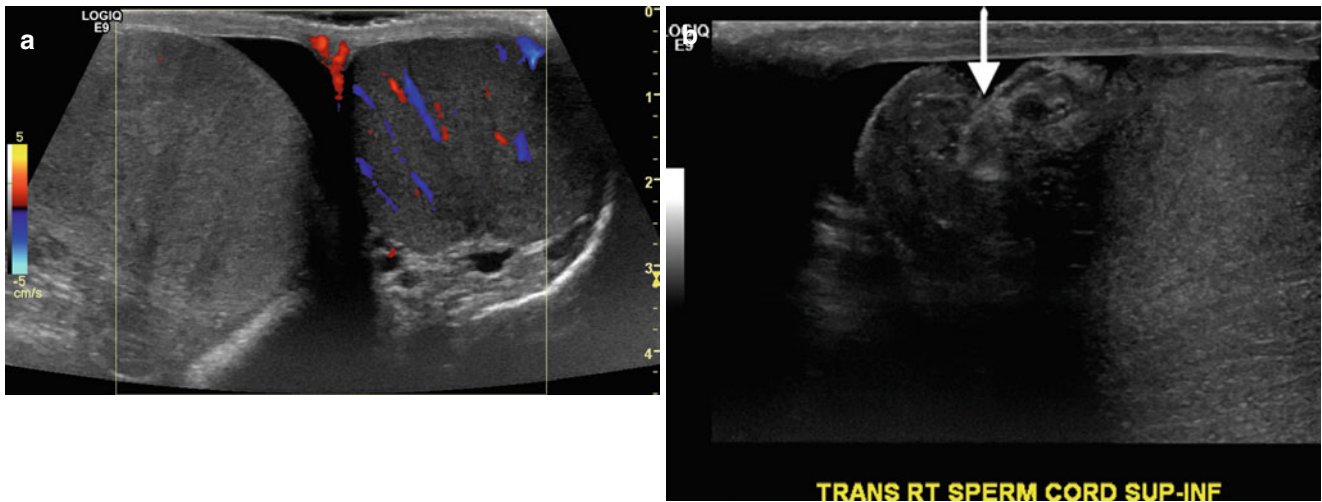
Fig. 2.8 Testicular torsion. Gray-scale and color Doppler images of the testes and gray-scale image of the spermatic cord in a young man presenting with acute right scrotal pain. (**a**) Color Doppler side-by-side transverse image demonstrates the absence of vascular flow to the right testicle compared the normal left testicle as manifested by the lack of color signal. (**b**) Transverse image demonstrating twisting of the spermatic cord (*arrow*)
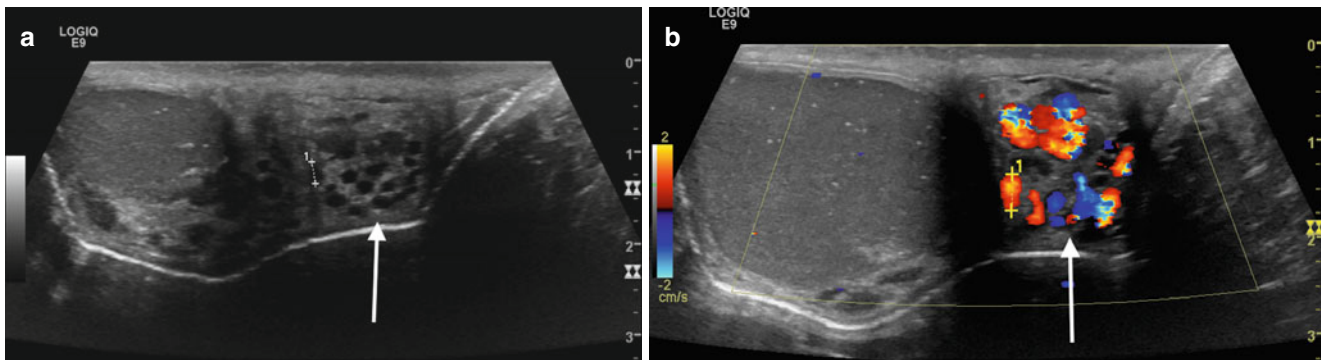

Fig. 2.9 Varicocele. Gray-scale (**a**) and color Doppler (**b**) sonographic images of the left testicle and an adjacent hydrocele. An extratesticular plexus of tortuous vessels (*arrows* (**a**, **b**)) is demonstrated with dilata-tion of the individual vessels upon Valsalva maneuver. Incidentally noted testicular microlithiasis can also be seen, manifested by scattered echogenic intratesticular foci

sels used by different authors, ranging typically from 2 to 3 mm. When utilizing color Doppler sonography at rest, blood flow within a suspected varicocele may be too slow for detection. With utilization of the Valsalva maneuver, the varicocele will enlarge and demonstrate reversal of flow. Color Doppler sonography is the accepted gold-standard technique for varicocele assessment as it provides accurate diagnosis and can also be used to stage lesions [18].

Computed Tomography (CT): Physical Principles and Genitourinary Applications

Physical Principles

The first CT scanner was developed by Sir Godfrey Hounsfield in Middlesex, Great Britain. In 1973, the first CT scanners were used clinically. Houndsfield and Allan Cormak were awarded the Nobel Prize in Medicine in 1979

for the development of CT technology [1, 19]. In the following decades, with constant advances in technology and computational power, cross-sectional imaging has revolutionized the practice of medicine, due to its capability to evaluate disease processes throughout the body in a noninvasive manner.

There are many urologic applications of CT, including, but not limited to, detection and characterization of renal stone disease; obstructive uropathy; benign and malignant tumors of the adrenals, kidneys, and upper and lower urinary tracts; traumatic injury; infection and its complications; and assessment of renal artery disease. Technologic advances over the years have greatly increased the capabilities of CT and have resulted in markedly greater speed of acquisition, anatomic coverage, and the ability to obtain dynamic contrast-enhanced images, all of which have worked to increase its diagnostic accuracy and image quality. This has also led to the development of newer applications, such as dual-energy CT, CT angiography, and CT urography. A drawback to the use of CT is its use of ionizing radiation, which results in a relatively large radiation dose. In recent years, however, dose reduction techniques have been implemented on a wide-scale basis, which have the potential to significantly reduce the dose from routine CT imaging.

A fundamental limiting factor of plain film radiography is that a three-dimensional object is reduced to a two-dimensional image, with the potential for multiple structures of varying radiodensity to be superimposed on one another, with the potential for the anatomy of interest to be obscured. Two distinct and extremely important advantages of CT over plain film radiography are (1) acquisition of a cross-sectional image with removal of any superimposed structures and (2) almost complete elimination of radiation scatter, which results in much greater sensitivity to differences in x-ray attenuation, thereby allowing excellent contrast between soft tissue structures. A CT examination is made up of multiple images, each one containing visual information from narrow anatomic sections through the imaged section of the body. The penetrating x-ray beam is collimated (shaped) into a very precise width [1, 19].

CT scanners are made up of two major components: the scanning component and computer components. The gantry consists of the scanning components, which surround the central aperture through which the patient is scanned. The computer components are located in the CT scanner control room. The scanning component includes the generator or power source, x-ray tube, collimators, detectors, data acquisition system computer components, image reconstruction, and scanner console.

Each detector, along with the focal spot of the x-ray tube, defines a ray. The detector measures the intensity of the x-rays within its ray. The intensity of the beam within each ray depends on the amount that x-rays are attenuated in the tissue through which it passes. Attenuation is a measurement of the fraction of radiation removed in passing through tissue. The attenuation of each boxlike element, or voxel, in the plane being scanned is measured by using many different rays acquired from many different angles over the course of the scan. The linear attenuation coefficient of a material indicates how strongly it absorbs or scatters (attenuates) x-ray photons. The linear attenuation coefficient depends on three properties: atomic number, physical density, and photon energy. The creation of a CT image is reliant upon the different attenuation characteristics of various tissues in the body [1, 19].

Once image detectors have assembled the data from each ray, images are reconstructed via analytical and iterative methods. The most commonly used reconstruction method is filtered backprojection, which has been used in the earliest CT scanners and is still used today. Filtered backprojection essentially determines the average density of each pixel by collecting sets of rays called projections, which are made across the patient in a particular direction in a section plane. Multiple projections are needed to determine average attenuation at each point, using rotational intervals of less than 1° [1, 19].

CT images are composed of gray-scale values, with each element of the image (pixel) assigned a gray-scale value dependent upon its average attenuation. Denser materials will cause greater attenuation of photons and will be brighter (whiter) on the CT image, while images that are less dense will be darker (blacker). Density measurements are standardized using the Hounsfield scale, in which water has a Hounsfield unit of zero, with other tissues ranging from −1000 (air) to +2000 (bone). Any voxel that has attenuation greater than water will have a positive HU value, and voxels which have attenuation less than water will have a negative HU. An attenuation value of specific tissue can be easily obtained by placing a cursor over the region of interest (ROI) at the workstation, for which the computer can average the attenuation of the voxels within the cursor. Attenuation values play great importance in tissue characterization and diagnosis and must be precisely calibrated on a regular basis [1, 19].

Detector arrays in multislice scanners are two dimensional. The number of detectors in the z-direction (in the head-to-toe direction of the patient) determines the maximum number of slices which can be simultaneously acquired. In a single-slice scanner, the slice width is determined by the width of the collimator. In multislice scanners, the slice width is determined by the width of the individual detectors. For instance, in a system with 64 detectors which are 0.625 mm in width, the slice thickness is 0.625 mm [19]. In actual practice, thicker slices are usually reconstructed for routine interpretation; however, thin sections are stored at the CT workstation and are available for review, if necessary.

Many imaging acquisition parameters determine image quality and patient dose. Two important acquisition parameters that affect radiation dose and image quality are peak tube voltage (kVp) and effective mAs. The effective mAs is the tube current (milliamperes) multiplied by the length of time that a given point in the patient is in the beam (seconds). The energy of the most energetic x-ray photon in the beam is always equal to the kVp. Pitch is another important acquisition parameter: this refers to the table movement per tube revolution divided by the beam width. Adjustments in pitch affect scan time, z-axis resolution, and radiation dose [1, 19].

Prior to the introduction of helical CT technology, scanners operated in axial or incremental mode. In axial CT scanners, the CT table is stationary during image acquisition, with the tube and detectors making one complete rotation. The x-ray beam is then turned off and the table repositioned [1, 19].

The design of modern CT scanner has been modified so that there are no hardwired connections between the generator and x-ray source and between the detector array and computer. This is achieved by slip-ring technology. Slip-ring technology, as well as advances in x-ray tube design and computer speed, made the development of helical scanning possible. Helical CT allows for uninterrupted motion of the x-ray source and the detector array, which rotate in a complete 360° arc around the patient. Simultaneously, the CT table (and patient) is moving in a continuous manner and at a predetermined speed [1, 19]. The result of these two different movements is that the beam takes a helical path through the patient. Helical scanners are capable of much faster scanning times and thinner slice acquisition than incremental CT scanners [19]. This improved temporal resolution has enabled dynamic studies after the administration of a bolus of intravenous iodinated contrast, whereby the entire abdomen and pelvis can be scanned on the order of seconds and images can be obtained in various phases of interest for a particular indication. For example, a typical examination for the evaluation of a renal mass would include arterial, nephrographic phases and sometimes excretory (pyelographic) phases as well as an unenhanced acquisition.

Dual-Energy CT

Dual-energy CT (DECT) scanners are built with two x-ray source/detector arrays. The tube voltage (kVp) settings for the two sources differ, resulting in two separate attenuation maps for the same object, one at a high energy level and one at a low energy level. As mentioned above, the linear attenuation coefficient of a specific material is dependent upon three properties: atomic number, density, and photon energy. DECT uses information obtained from both the high and low energy arrays to assess the rate of change in the linear attenuation coefficient of the structure being analyzed. As various elements and compounds commonly found in the human body have unique linear attenuation curves over a spectrum of energy, DECT is capable of providing information regarding specific chemical composition [20].

There are several ways in which the data obtained from DECT can be exploited to provide useful clinical and diagnostic information. Material-specific images can be formed by targeting a specific material's linear attenuation curves and removing it from the image. Common base materials targeted by DECT include water, iodine, and calcium. As enhancement on CT is produced from the effects of iodinated contrast medium, subtracting iodine results in a "virtual" non-contrast image, so that a single dual-energy scan could potentially replace two single-energy scans (pre- and post-contrast) [20]. This could have application in the evaluation of renal masses, calculous disease, adrenal nodules, and any other scenario where non-contrast images are necessary for lesion characterization or visualization. An additional benefit of virtual non-contrast images would be radiation dose reduction, due to elimination of a separate unenhanced acquisition.

Conversely, iodine-specific data sets (iodine maps) can be obtained. These are composed exclusively of the contribution of iodine to the image and may also be efficacious in renal mass characterization and other scenarios [21]. By enabling better visualization of iodine signal, enhancement within a mass may be more easily diagnosed on iodine-specific images. Studies have so far shown promising results for the use of virtual non-contrast and iodine-specific images in differentiating cystic from solid renal masses [21–23]; however, these techniques will require further study and validation. Future advances and refinements in dual-energy technology may even surpass the diagnostic capabilities of conventional, single-source CT.

Virtual non-contrast images have also shown promise in characterizing adrenal nodules [24, 25]. This is a promising development given the high frequency of adrenal nodules found on contrast-enhanced CT scans, which often need repeat CT examination with unenhanced images to better characterize.

Another active area of investigation of DECT is in renal stone characterization. DECT makes use of the distinctive absorption patterns of various stone components at both high and low energy levels to identify specific chemical composition [20]. This can expedite the work-up of renal stone disease, which can often involve lengthy laboratory and imaging investigation. Knowledge of stone composition can help improve treatment, as management of different stone types differs. DECT has shown to be reliable in differentiating uric acid stones from non-uric acid stones [20] and shows promise in the differentiation of other calculi (cystine, struvite, calcium oxalate monohydrate/calcium oxalate dihydrate/brushite, and hydroxyapatite/carbonate apatite calculi) [26, 27].

Applications of CT in the Urinary Tract

Kidneys

There are numerous indications for the use of CT in the evaluation of renal pathology. Some of the more common reasons include renal mass characterization, renal cancer staging, stone disease, trauma, inflammatory/infectious processes, obstructive uropathy, vascular disease, congenital urinary tract anomalies, and postoperative evaluation.

CT is a highly accurate modality for renal mass evaluation. Since the differential diagnosis often revolves around differentiating between a cystic and solid mass, the key element of such evaluation is the presence or absence of contrast enhancement [28]. Benign renal cysts are typically uniformly low in density (at or near the attenuation of water) on CT, with an imperceptible wall and no septations or mural nodules; however a significant minority will appear as high-attenuation lesions on CT due to the presence of hemorrhagic or proteinaceous debris. Because the density of these lesions (greater than 20 HU) overlaps with solid nodules, they cannot be differentiated by unenhanced or contrast-enhanced CT alone. Rather, both unenhanced and enhanced images must be acquired in the same sitting, with HU measurements obtained from both series. At this time, there is no true consensus on what constitutes significant enhancement; however, a threshold of >20 HU is used by some experts, with a 10–20 HU difference considered to be equivocal [28]. In the case of an enhancing soft tissue mass with no visible fat, there are no reliable CT findings to help differentiate a benign soft tissue mass, such as an oncocytoma or lipid-poor angiomyolipoma, from a renal cell carcinoma (RCC). Lymphoma and metastatic disease can also have a similar appearance to RCC, and attention to medical history and extrarenal findings must be made in order to make an accurate diagnosis. Nonneoplastic mimics of renal cell carcinoma include focal pyelonephritis, "pseudotumor" arising from congenital lobulation of the renal contour or from normal parenchyma adjacent to scarred cortex, and IgG-4 disease [29].

Artifacts, such as beam hardening from a patient who is unable to position his/her arms away from their sides or from pseudoenhancement, can give spurious results. Pseudoenhancement is a well-known artifact on CT, which causes increase in attenuation measurements in renal lesions on intravenous contrast-enhanced CT. This is due to an incorrect image reconstruction algorithm in areas adjacent to high-attenuation structures (in this case, the avidly enhancing renal parenchyma), with small, intraparenchymal lesions most likely to be affected [30, 31].

Cystic renal lesions are ubiquitous in the adult population, with simple cysts comprising the overwhelming majority of these masses. Cystic neoplasms do, however, arise in the kidney; therefore, the density (HU) measurement and internal composition of all cystic renal masses must be carefully assessed. The presence of enhancing septations and nodules increases the likelihood of a cystic neoplasm. The Bosniak classification of cystic renal masses categorizes lesions based on their morphology. Bosniak criteria include density, number, and thickness of septations; wall thickness; and soft tissue nodules (Fig. 2.10). The presence or absence of enhancement must be carefully assessed, as benign hemorrhagic cysts can have many of the features of a cystic neoplasm; however, any internal components should not enhance [28].

Angiomyolipomas are well assessed on CT and can be diagnosed when a renal mass contains macroscopic fat. This is a key element of renal mass characterization, as it is extremely rare for a renal cell carcinoma to contain fat. An unenhanced thin-section CT is the most sensitive test for fat detection and should be performed if fat is suspected in an enhancing renal mass. A small minority of angiomyolipomas will either contain no fat or an insufficient amount of fat to be detected at CT. Although these lesions often have features on CT that may suggest the diagnosis, they cannot be reliably distinguished from renal cell carcinoma without biopsy or surgery [28].

In cases of known renal malignancy, CT is an accurate modality for staging. The renal vein and IVC can be assessed for the presence and extent of tumor invasion. Tumor thrombus can often be distinguished from bland thrombus by enhancement in the former; however, there are limitations of both CT and MRI in assessing for invasion of the IVC wall, which can significantly impact prognosis [32]. Lymph node status is assessed based primarily on node size, with a cutoff of 1 cm in short axis diameter. This inevitably results in some false-positive (enlarged but benign nodes) and false-negative
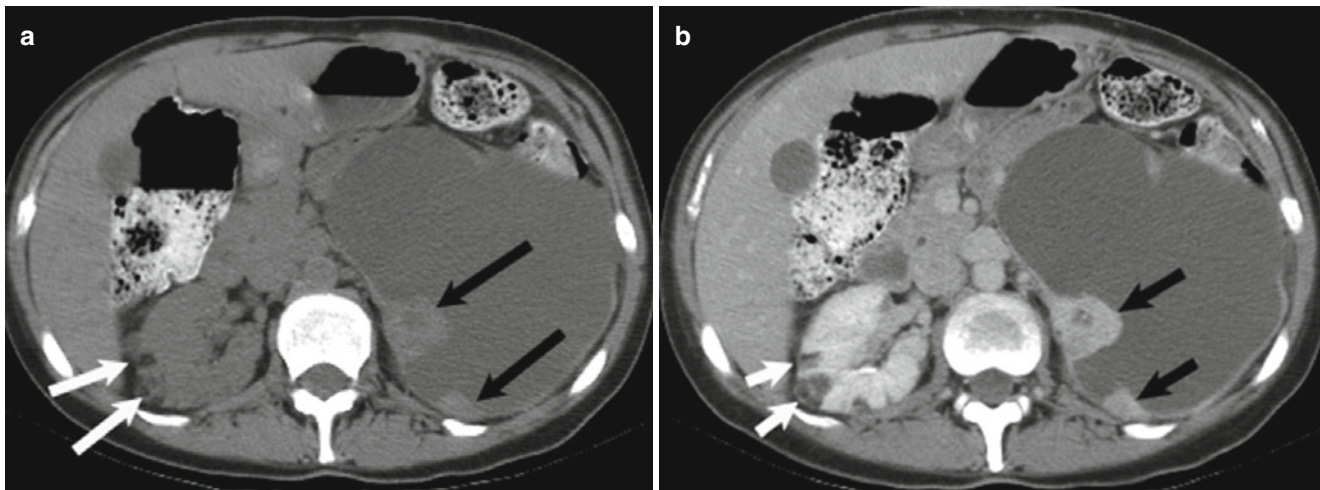
Fig. 2.10 Cystic renal cell carcinoma. Axial unenhanced (**a**, **b**) contrast-enhanced CT images demonstrates a large cystic left renal mass with nodular enhancing components (*black arrows*). Enhancement within a renal mass must be confirmed by comparison with unenhanced CT images. Also note two small fat density right renal lesions representing angiomyolipomas (*white arrows*)

(small but malignant nodes) cases. Johnson et al. reported a sensitivity of 83 % and specificity of 88 % for nodal assessment in the setting of renal cell carcinoma [33]. Distant metastases to the lung, liver, bone, and other sites are well depicted on CT.

In most cases of acute pyelonephritis, imaging is not necessary for diagnosis or management; however, CT does have a role in select subgroups of patients. These include those at high risk of complications, such as the immunocompromised, including diabetics, patients in whom there is poor response to standard treatment regimens, and in patients where there is clinical suspicion for complications, such as renal abscess, pyonephrosis, or emphysematous pyelonephritis (Fig. 2.11) [34, 35]. The typical finding on intravenous contrast-enhanced CT is one or multiple wedge-shaped areas of cortical hypoenhancement, reflecting involved areas of renal parenchyma (Fig. 2.12). Radiating linear bands of alternating decreased and normal enhancement, likely due to obstructed tubules with intervening normal tubules, can give rise to a "striated nephrogram." Secondary findings include global renal enlargement, thickening of Gerota's fascia, and urothelial thickening of the renal pelvis and ureter [34, 35]. CT can also demonstrate renal manifestations of less common infections, such as tuberculosis, fungal organisms, echinococcus, and xanthogranulomatous pyelonephritis (Fig. 2.13) [35].

Because of its availability, rapid patient throughput, and accuracy for diagnosing renal injury, CT is the first-line modality for the evaluation of blunt or penetrating renal trauma, including iatrogenic injury from surgical and percutaneous renal procedures. CT findings can be graded in conjunction with a renal trauma grading system, such as the American Association for the Surgery of Trauma (AAST)

[36–38]. Intravenous contrast is essential when CT is used for renal trauma evaluation, in order to accurately demonstrate injuries to the kidney parenchyma and vasculature as well as perirenal and retroperitoneal hemorrhage (Fig. 2.14) and fluid collections. Excretory (delayed) phase images are necessary to evaluate for collecting system injury (AAST grade IV or V), which is diagnosed by extravasation of contrast-opacified urine from the damaged segment of the collecting system (Fig. 2.15) [38].

CT has become the gold standard for the evaluation of renal stone disease, replacing excretory urography and plain radiographs in most centers. CT has been shown to be highly sensitive (95–98 %) and specific (96–100 %) for diagnosing urolithiasis [39–41]. It is also readily available in most emergency departments, rapidly performed, does not require oral or intravenous contrast, and can detect stones of all sizes. CT can also help provide alternative diagnoses to stone disease either within (infection, neoplasm, congenital anomalies) or outside (e.g., pancreatitis, appendicitis, etc.) the urinary tract. The most direct sign of ureterolithiasis is the identification of a stone in the ureter. Secondary signs of an obstructing stone commonly seen on CT include hydroureteronephrosis and perinephric and periureteral fat stranding [42].

CT can provide essential information in patients undergoing stone removal procedures such as percutaneous nephrolithotomy (PCNL), ureteroscopy, or extracorporeal shock wave lithotripsy (ESWL). The preprocedure scan can help ascertain a safe route for needle access and the most appropriate calix to puncture in a patient undergoing PCNL and provide a stone to skin (SSD) distance prior to ESWL. Post-intervention CT can be used to assess for any residual calculi or obstruction [43].

Fig. 2.11 Emphysematous pyelonephritis. Coronal unenhanced CT image demonstrates a wedge-shaped focus of gas (*arrows*) within the parenchyma of the left kidney
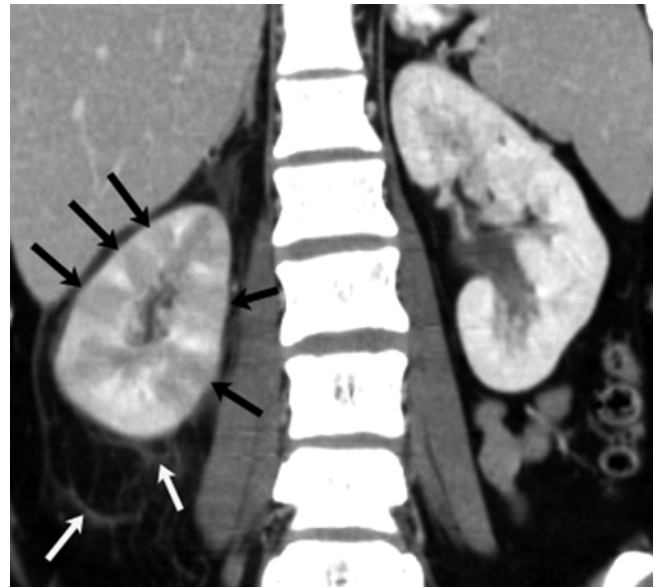

Fig. 2.12 Pyelonephritis. Coronal reformatted image from CT performed with intravenous contrast demonstrates multiple wedge-shaped areas (*black arrows*) of parenchymal hypoenhancement and perinephric stranding (*white arrows*)
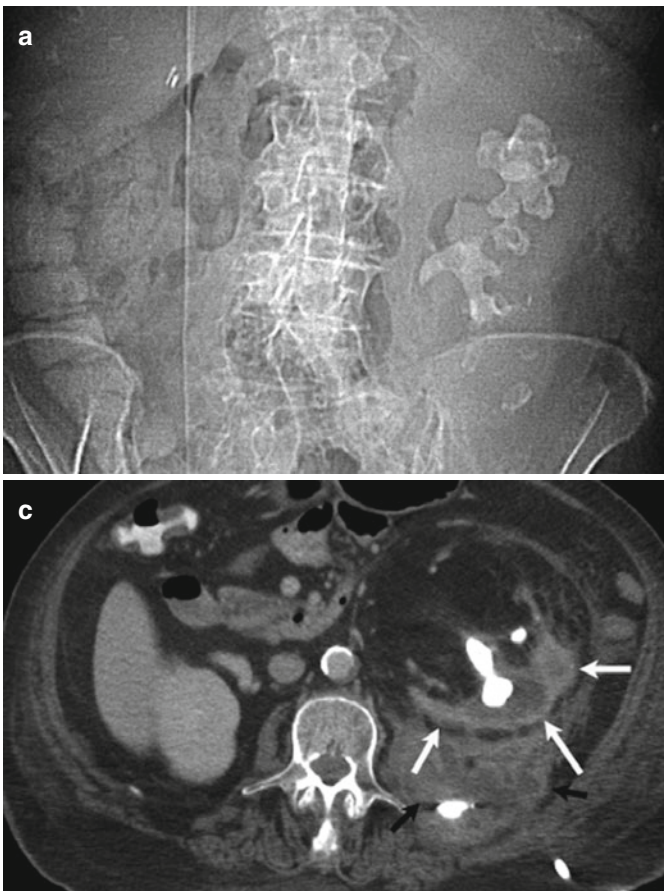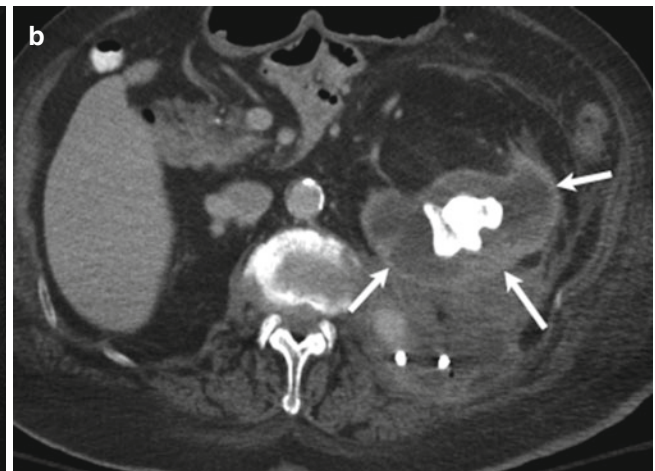

Fig. 2.13 Xanthogranulomatous pyelonephritis. Scout CT view (**a**) shows a large left staghorn calculus. Axial images from contrast-enhanced CT (**b**, **c**) demonstrate a nonfunctioning, hydronephrotic kidney (*white arrows*). Note abscess (*black arrows*) with drainage catheter in the posterior retroperitoneum

Congenital urinary tract anomalies are well evaluated with CT and often detected incidentally in the adult population; however, MRI is the preferred modality for the assessment of a known or suspected anomaly in a child due to the lack of ionizing radiation and the ability to perform a multiparametric examination.

Adrenal Glands

CT can be used to both characterize adrenal lesions and as a tool for surveillance of stability of an indeterminate nodule. The most common adrenal nodule is the adenoma. Due to their high frequency in the general population, these are often discovered as incidental findings on CT performed for other indications [44–46]. CT can be used to characterize a lesion as a benign adenoma in two manners. The first and simplest is by performing unenhanced CT. The majority of adenomas will contain intracellular lipid, which will reduce the attenuation of the nodule. Adrenal nodules measuring less than 10 HU on unenhanced CT can be diagnosed as adenomas with a 71 % sensitivity and 98 % specificity as reported in a meta-analysis by Boland et al. [47]. Unfortunately, about 30 % of adenomas will not meet this criterion. These so-called "lipid-poor" adenomas can be evaluated with a combined unenhanced and contrast-enhanced CT examination with washout analysis. Adenomas will usually have more rapid contrast washout than malignant nodules. The histopathologic basis for this is thought to be disorganized angiogenesis and vascular permeability in malignant nodules, leading to extravascular contrast leakage. Washout is calculated by comparing density measurements made on all three phases of the examination (unenhanced, dynamic contrast-enhanced, and delayed images obtained 15 min after contrast administration.) Established washout thresholds for the diagnosis of an adenoma are greater than 60 % absolute percentage washout $(([HU_{contrast} - HU_{delayed}]/[HU_{contrast}-HU_{unenhanced}]) \times 100)$ or greater than 40 % relative percentage washout $(([HU_{contrast}-HU_{delayed}]/[HU_{contrast}]) \times 100)$. Using these

Fig. 2.14 Renal injury with active bleeding. Contrast-enhanced coronal reformatted CT image demonstrates a full-thickness laceration of the left kidney. There is a large retroperitoneal hematoma (*arrows*) containing high-attenuation foci, representing vascular contrast extravasation (*arrowheads*)
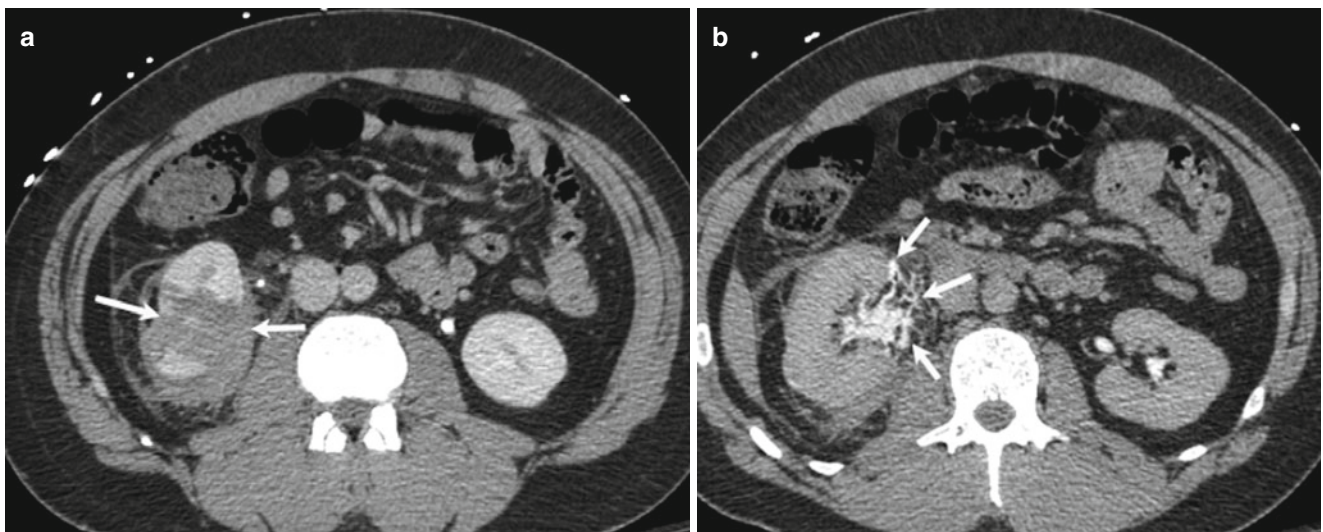

Fig. 2.15 Grade IV renal trauma. Axial contrast-enhanced images obtained in the nephrographic (**a**) and excretory (**b**) phases show a large parenchymal laceration (*arrows*, **a**) and extravasation of excreted contrast (*arrows*, **b**) diagnostic of collecting system injury

criteria, Caioli et al. successfully diagnosed 160/166 adenomas with 98 % sensitivity and 92 % specificity [48]. One important caveat to remember in adrenal washout imaging is that a pheochromocytoma can demonstrate washout levels similar to that of an adenoma. Such a lesion may be suspected if its absolute enhancement exceeds 110–120 HU after contrast administration [49].

Adrenal myelolipomas can be easily diagnosed in most cases due to the presence of macroscopic fat. Adrenal cysts are uncommon lesions, most often pseudocysts due to chronic hematoma. These lesions often demonstrate low attenuation and may contain wall calcification [44].

Other adrenal masses include hemorrhage, ganglioneuroma, metastatic disease, pheochromocytoma, adrenal cortical carcinoma, lymphoma, and collision tumor, as well as neuroblastoma in the pediatric population. Significant overlap exists in the CT features of these lesions, and further investigation with laboratory tests and possibly biopsy may be necessary to make an accurate diagnosis. Contrary to prior literature suggesting that ionic intravenous contrast administration may provoke a hypertensive crisis in patients with a pheochromocytoma [50], more recent studies have shown no adverse effects to nonionic intravenous contrast in patients with pheochromocytoma [51, 52].

Adrenal cortical carcinoma has a propensity for venous invasion, the extent of which can be characterized on contrast-enhanced CT scan. An adrenal mass with invasion of the inferior vena cava is highly suggestive of adrenal cortical carcinoma [53]. There are numerous causes of nontraumatic adrenal hemorrhage, which can mimic an adrenal tumor on imaging studies. Hemorrhage may be suspected in an adrenal mass with high attenuation on unenhanced imaging, with or without stranding of the periadrenal fat. The possibility of an underlying hemorrhagic neoplasm must also be entertained and can be further investigated using contrast-enhanced MRI with subtraction imaging [44].

Ureters and Bladder

With the exception of stone disease as discussed above, CT evaluation of the ureter usually necessitates IV contrast administration. Common indications for imaging of ureteral disease include hematuria, suspected tumor, known lower tract or previously treated upper or lower tract transitional cell carcinoma, investigation of ureteral obstruction, and after urinary diversion surgery. Comprehensive assessment of both the upper and lower tracts with CT is performed with CT urography. CT urography is usually performed as a triphasic study, with acquisition of unenhanced, nephrographic, and excretory phase series. Diuretic administration,

typically low-dose intravenous furosemide, aids in the visualization of the upper and lower tracts by diluting the excreted contrast and increasing ureteral distention [54]. A biphasic study can be performed in younger patients to decrease radiation dose by using a "split bolus" technique, whereby a combined nephrographic and excretory series is obtained. This is accomplished by dividing the contrast volume into two doses: a smaller dose of 30 and 50 cc of contrast administered 8–10 min prior to scan initiation, with the remainder (approximately 100 cc) given 2 min prior to the scan (this technique allows time for the earlier dose to circulate and become excreted by the kidneys), while the second dose serves to provide a nephrographic phase [55]. Properly performed CT urography allows for detailed evaluation of the kidneys, collecting systems, ureters, and bladder and has been shown to be superior for the detection of transitional cell carcinoma as compared with excretory urography, with a meta-analysis finding a pooled sensitivity of 96 % and pooled specificity of 99 % [56]. Tumors will appear as a filling defect or wall thickening (either eccentric or circumferential) in the contrast-opacified collecting system (Fig. 2.16), with or without hydroureteronephrosis. In positive cases, CT allows for tumor staging to be performed simultaneously [54].

Other indications for CT urography of the ureters include trauma, including iatrogenic trauma from surgery or endoscopic urologic procedures, and infectious and inflammatory disorders (Fig. 2.17). CT urography can depict congenital anomalies, such as ureteropelvic junction obstruction, ureteric webs, duplicated collecting system, and megaureter, with excellent detail [54], although, as mentioned above, MRI, if available, is the preferred modality for such indications in the pediatric population.

Cystoscopy is typically the first-line method for the diagnosis of bladder tumor. When CT is performed for bladder tumor assessment, CT urography is indicated, in order to evaluate both the upper and lower urinary tracts, due to the tendency of urothelial neoplasms to be multicentric, with both synchronous and metachronous urinary tract involvements. There is the potential for some bladder tumors to be better visualized on the dynamic contrast-enhanced phase of the CT urogram rather than the excretory phase because (a) bladder cancers have been shown to have robust enhancement in the early phase of contrast administration [57] and (b) nonuniform opacification of the bladder due to mixing of contrast and urine can obscure or mimic a bladder nodule [58]. Sadow et al. reported a sensitivity of 79 % and specificity of 94 % for bladder cancer detection utilizing CT urography technique [59]. Limitations include underdistention of the bladder obscuring or potentially mimicking a tumor and flattening of the tumor from an overdistended bladder. CT
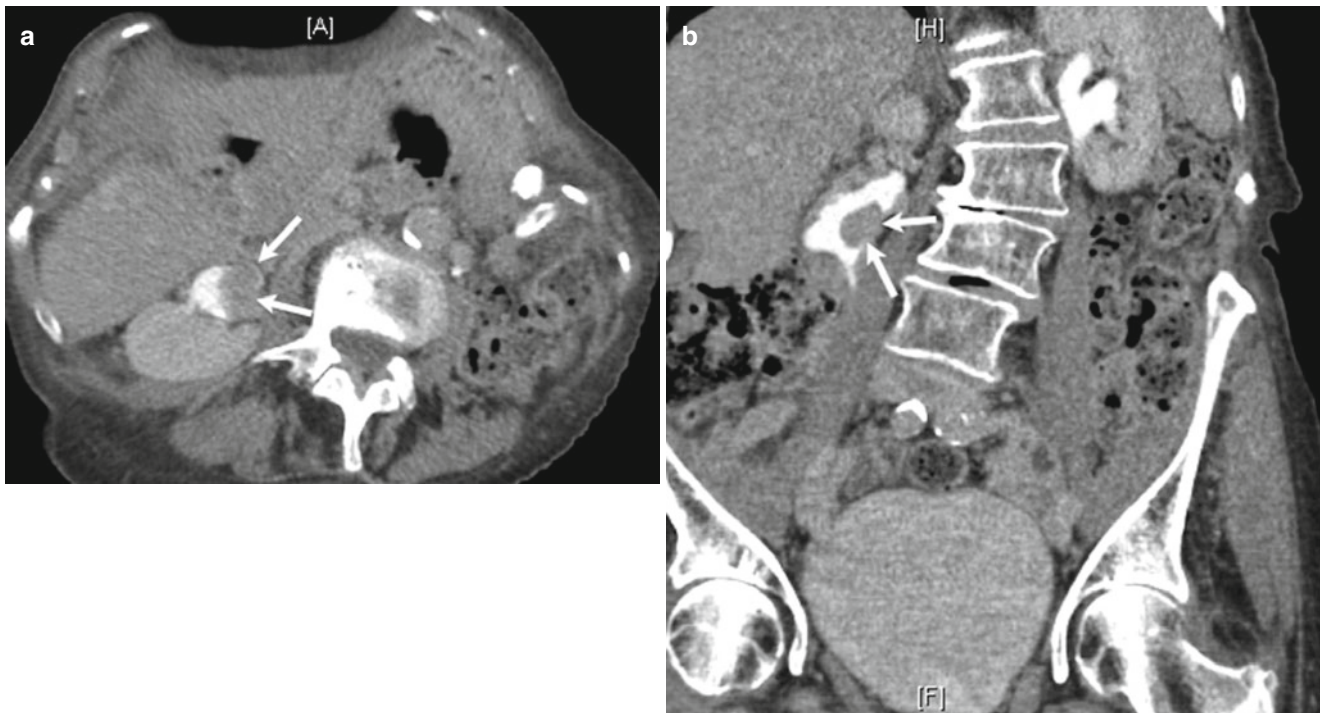
Fig. 2.16 Renal pelvis mass. Axial (**a**) and coronal (**b**) excretory phase images from CT urogram demonstrates a polypoid mass in the left renal pelvis (*arrows* (**a**, **b**)), outlined by opacified urine. This finding is suspicious for transitional cell carcinoma; however, tissue confirmation was not obtained due to the advanced age and comorbidities of the patient

may help visualize cancer within a bladder diverticulum, especially when the diverticulum is not accessible by cystoscopy (Fig. 2.18) [60].

CT is useful for detecting macroscopic extravesical tumor spread (T3b disease) from organ-confined tumor, although it will not detect microscopic perivesical fat invasion (T3a disease). CT can also be used to detect pelvic and retroperitoneal lymphadenopathy and distant metastatic deposits. Invasion of local organs, such as the prostate and rectum, can also be evaluated, although the lack of clear fat planes in the inferior pelvis can be a limiting factor in this regard. The inability of CT (and MRI) to resolve specific layers of the bladder wall significantly limits its overall accuracy in staging, especially between T1, T2, and T3 disease [29].

In addition to tumor detection and staging, other indications for CT of the bladder include trauma, fistulous disease, and assessment for rupture after biopsy, surgical procedure, or other instrumentation. Definitive evidence of bladder injury can be obtained with CT cystography which will show extravesical contrast extravasation in cases of bladder perforation and can also demonstrate whether the perforation is intra- or extraperitoneal, depending on the anatomic location of the extravasated contrast (Fig. 2.19). In the setting of blunt trauma, CT cystography has been shown to be accurate in demonstrating bladder rupture, with both sensitivity and specificity approaching 100 % [61, 62].

Magnetic Resonance Imaging: Basic Physics and Genitourinary Applications

Magnetism is an invisible force in nature, associated with the Earth, as well as many natural materials. Moving charges in an electric current flowing through a wire can produce a magnetic field. The unit of strength of a magnetic field is the tesla, with magnetic field strengths used in clinical MRI of approximately 0.5–3 T.

Protons also have a tiny associated magnetic field as a result of a spinning charge. This tiny magnetic field, called the magnetic dipole moment, can experience a force from an externally applied magnetic field. Biologic tissues are mostly composed of water molecules, which contain two hydrogen ions each consisting of a single proton. Clinical MRI applies to magnetism resulting from the proton, although electrons and neutrons have associated magnetism as well. In atomic nuclei with greater than one proton, protons will align with one another with opposite poles attracting. Pairs of protons with their unlike magnetic poles attracting lower the net magnetization of the pair. Thus, atoms with even atomic numbers will have no net magnetization.

Normally, the magnetic dipoles of hydrogen protons in tissue are randomly oriented. When exposed to an externally applied static magnetic field, such as in a clinical MRI magnet, the magnetic dipole will experience a force. The North pole of the hydrogen proton will be forced to align
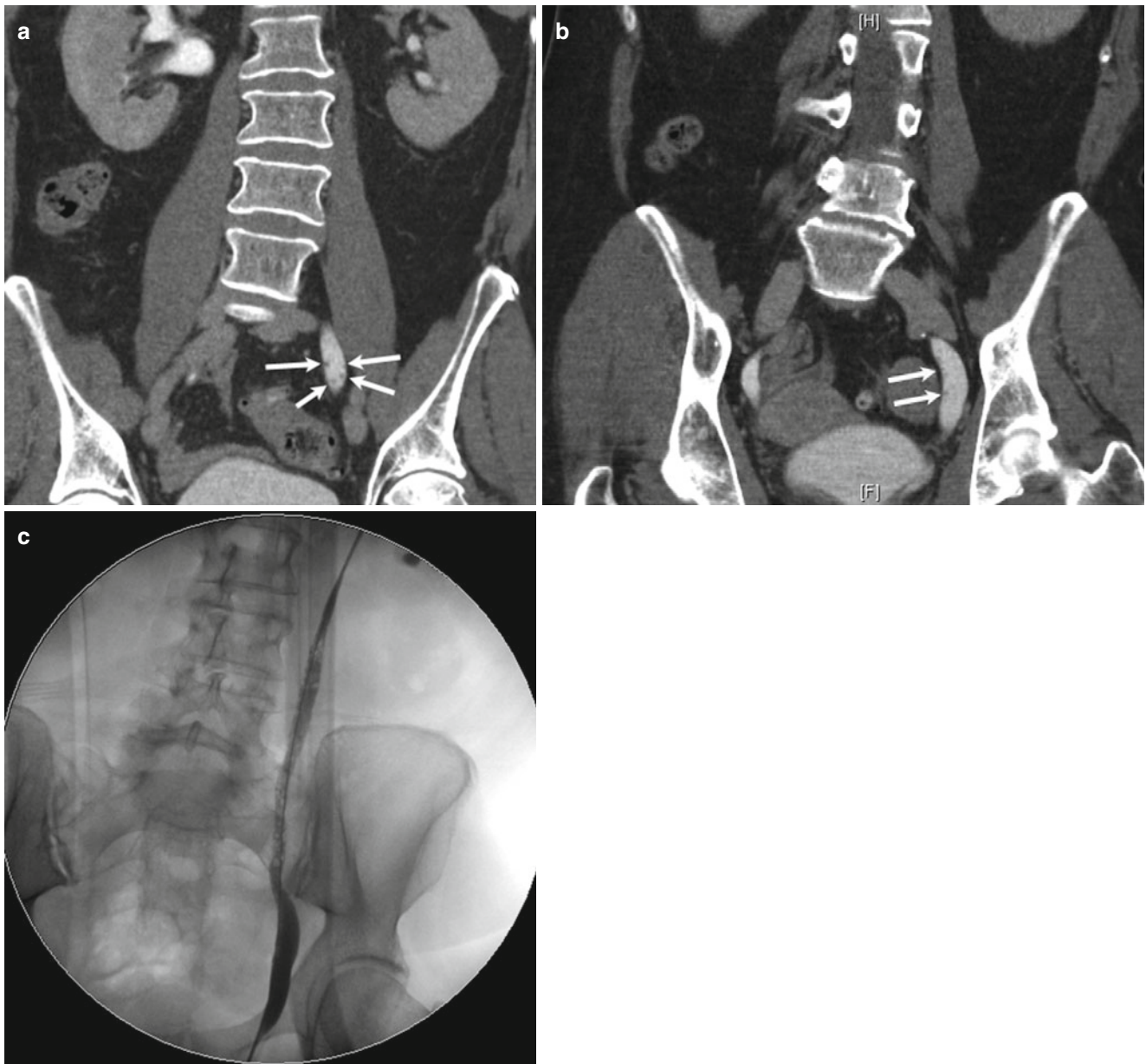
Fig. 2.17 Ureteritis cystica. Coronal images (**a**, **b**) from CT urogram demonstrate numerous tiny ureteral filling defects (*arrows*). Intraoperative fluoroscopic image obtained during retrograde pyelo-gram (**c**) better demonstrates the extent of ureteral involvement, with countless small intraluminal filling defects now visible

with the South pole of the external magnetic field. The proton is also forced into a spinning, precessional motion around the lines of the force of the external magnetic field, similar to that of a spinning top. The speed of proton precession, or precessional angular frequency (w), is influenced by the strength of the magnetic field and is known as the Larmor frequency. The relationship between proton precessional frequency and the external magnetic field is governed by the Larmor equation:

$$w = (y) \times (B0)$$

where (w) refers to the precessional angular frequency, (y) is the gyromagnetic ratio of the particular atom, and B0 is the strength of the external magnetic field.

When placed in a strong external magnetic field, protons are forced into parallel alignment, either with or against the direction of the magnetic field. A very slight majority of protons will align with the field, and it is this small excess which gives rise to MR signal, producing a vector (Mz) along the z-axis. This is known as the longitudinal vector.

In clinical MRI, a radiofrequency (RF) pulse in the same frequency range as the precessing protons is applied long
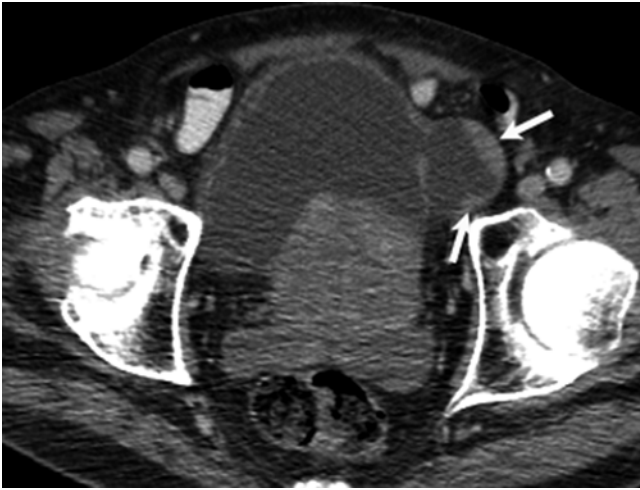
Fig. 2.18 Urinary bladder diverticulum with tumor. Axial contrast-enhanced CT image shows a left-sided urinary bladder diverticulum with nodular wall thickening suspicious for cancer (*arrows*)

Fig. 2.19 Urinary bladder perforation. Sagittal reformatted image from CT cystogram shows a defect in the wall of the bladder at the anterior dome and intraperitoneal contrast extravasation (*arrow*). The bladder was injured during cesarean section

enough to deviate the protons to a prescribed angle from the external magnetic field, which varies but is often 90 or 180°. This angle is known as the flip angle. Once the pulse is turned off, protons will return to their original state, a process known as relaxation, which has two components. The first is termed T1 relaxation and is defined as the time for the longitudinal magnetization to regain 63 % of its maximum value. Different tissues have different values of T1 and relax at different rates, with a short T1 relaxation time for adipose tissue and long T1 relaxation time for CSF.

The second effect of the applied RF pulse is that protons will synchronously precess, creating net transverse (Mxy) magnetization. Once net transverse magnetization is established and the RF pulse is turned off, protons will gradually precess in a more random fashion. Some protons will precess

faster and others slower, a process called dephasing, resulting in decay of the Mxy vector, termed T2 relaxation. T2 relaxation time of tissue is the time it takes for the Mxy vector to decay to 37 % of its maximum value. Different tissues have different values of T2 and dephase at different rates, with short T2 relaxation time for the liver, muscle, and myocardium and long T2 relaxation time for CSF [63].

Image Formation

In addition to a static external magnetic field, the process of image formation requires the introduction of magnetic field gradients (slopes of magnetic strength), which are changes in the magnetic field strength as a function of location in the patient. Under the influence of a magnetic field gradient, resonant frequency of protons affected by the gradient varies according to location. Three different gradients are applied during image formation: slice-selection, phase-encoding, and frequency-encoding gradients, each of which is applied in one of the three spatial planes, with the information from each used to assign signal to a precise point on the image, or pixel, which is the term for the smallest resolvable unit of area on an image.

Assuming the patient is lying supine on the MRI table, gradient direction can be applied anterior to posterior, superior to inferior, or left to right to create sagittal, axial, and coronal spatial information. Initially, a slice-selection gradient is turned on, and an RF pulse with a specific bandwidth is administered to the patient, and tissue with a resonant frequency within this bandwidth is excited. The thickness of the section of tissue excited by the pulse determines the actual slice thickness and is inversely proportional to the strength of the gradient.

Subsequently, in the excited slice, a gradient is applied along the phase-encoding axis. Protons in the excited slice will be precessing at different speeds along the direction of the gradient. Protons precessing faster gain phase. After the phase-encoding gradient is turned off, the frequency-encoding gradient is applied along an axis perpendicular to the phase-encoding axis. The phase- and frequency-encoding gradients encode proton magnetic moments spatially, essentially labeling each pixel. During readout, the RF coil then detects the magnetization signal as a summation of all voxels which have each been uniquely labeled. Signal from each set of ensembles fills in one data point in k-space, which is then in turn processed into an image through Fourier transformation [63].

Pulse Sequences

An MRI pulse sequence diagram outlines the basic execution of an MRI scanner as follows: RF excitation, slice-selection

gradient, phase-encoding gradient, frequency-encoding gradient, data acquisition. These pulses are repeated many times during MRI imaging. The time between repetitions of pulse sequences is the repetition time (TR). The time between the RF pulse and the greatest MRI signal from transverse magnetization is the echo time or TE. The TR and TE are important tissue-related parameters having impact on image contrast. The TR is selected by the MRI operator and impacts the level of T1 contrast between tissues. If the TR is long, T1 relaxation differences between tissues are minimized. A short TR allows for greatest T1 contrast between tissues; therefore, T1-weighted images employ short TRs. T2-weighted sequences utilize a long TR in order to decrease T1 contrast and a long TE to optimize T2 contrast between tissues. Tissues with short T1 times will be brighter on T1-weighted images, while tissues with long T2 times will have higher signal on T2-weighted sequences [64–66].

Spin Echo

Spin-echo and fast spin-echo sequences are the mainstay of conventional MR imaging. This sequence begins with a 90° RF pulse followed by a 180° refocusing pulse at time TE/2. The signal produced at time TE fills one row of k-space. At time interval TR, the whole process is repeated to fill subsequent rows of k-space. TR and TE affect weighting as described above and can be tailored to provide either T1- or T2-weighted sequences. Spin-echo sequences have low sensitivity to magnetic field inhomogeneities and magnetic susceptibilities due to the application of the above-described 180° refocusing pulse [64–66].

Due to the very long imaging times of spin-echo sequences, they have largely been replaced by fast spin-echo (FSE). FSE is a variation on spin echo, whereby multiple rows of k-space are filled in a single TR interval. This results in much faster imaging times, with similar image quality, signal, and resolution to conventional spin-echo sequences [65, 66].

Gradient-Recalled Echo (GRE)

These sequences, of which there are numerous variations, begin with a small (<90° flip angle) which tips longitudinal magnetization and creates some transverse magnetization. Unlike spin-echo imaging, a 180° refocusing pulse is not applied in GRE. A negative frequency gradient pulse causes rapid dephasing of transverse magnetization followed by a positive frequency gradient pulse which rephases transverse magnetization and produces a gradient echo at TE.

Due to the use of small flip angles and the lack of a refocusing pulse, GRE images can be obtained with extremely short TR and TE values, allowing for rapid acquisition times. GRE sequence times are measured in seconds, as opposed to spin-echo sequences, which take minutes to complete, thus allowing breath-hold imaging to be performed. GRE sequences are vital for imaging the upper abdomen and to a lesser degree the

pelvis, where fast sequences are necessary to minimize degradation from respiratory movements. GRE techniques also allow for volumetric imaging, including 3D magnetic resonance angiography and volumetric acquisitions [65, 67].

Inversion Recovery

This sequence begins with a 180° RF pulse causing inversion of the initial longitudinal tissue magnetization. A standard spin-echo sequence is then performed. During TI or inversion time, T1 relaxation causes different tissues to regain their longitudinal magnetization at different rates, which is the basis for T1 contrast. An inversion time (TI) can be chosen such that when a 90° spin-echo excitation occurs, a particular tissue magnetic moment will be at its "null point" and thus contribute very little to the overall signal. This property is utilized in short inversion time inversion-recovery (STIR) sequences for fat saturation and in fluid attenuated-inversion-recovery (FLAIR) sequences for saturation of water signal [64, 68, 69].

Diffusion-Weighted Imaging (DWI)

This is essentially a spin-echo T2-weighted sequence with a dephasing or diffusion-sensitizing gradient applied between the initial 90° RF pulse and the subsequent 180 pulse and a symmetric rephasing gradient applied after the 180° pulse. The basic idea behind DWI is to measure the degree of molecular motion during the time between these two gradients. DWI sequences can be performed with a range of B values. The B value refers to the strength of the diffusion-sensitizing gradient and is proportional to gradient amplitude, duration, and time interval between paired gradients.

The motion of water molecules in an environment of tightly packed cells or inflammatory debris will be restricted. Any change in phase acquired by the dephasing gradient is canceled by the rephasing gradient; thus signal from these tissues will be mostly preserved. Conversely, water molecules which are not restricted by their local environment can move relatively long distances after the initial gradient, and the effect of the first gradient will not be completely canceled out by the second gradient, resulting in net loss in signal intensity. In practice, this means that tissues with restricted diffusion will have higher signal than tissues with free diffusion. This difference in signal becomes more pronounced as the B value is increased. For instance, at a B value of 0, free water molecules have high signal intensity; signal and contrast from a B_0 image mirror that of a T2-weighted image. As the B value is increased, water molecules in a nonrestricted environment will lose their signal, while restricted tissues retain their signal.

Quantitative analysis of diffusion properties can be performed by the generation of apparent diffusion coefficient (ADC) maps, which are routinely obtained in clinical practice. Note that signal on the ADC maps is the opposite of

what is on the actual diffusion images described above: areas of restricted diffusion will be dark, while tissues with free diffusion will have bright signal [70, 71].

Fat Suppression

Due to differences in their local molecular environment, protons in fat have a slightly different resonant frequency than do protons in water. Fat suppression refers to the application of an RF pulse at the resonant frequency of fat protons, which selectively suppresses fat signal. Removal of high-signal fat has two important benefits in abdominal MR imaging. The first, more general benefit, is that fat suppression results in an image which is more sensitive to signal intensity differences, either from innate tissue properties or from contrast enhancement. This results in increased conspicuity of pathologic processes and enhancement. For these reasons, frequency-selective fat-suppressed imaging has become an essential element of the abdominal MRI exam.

A second and more specific benefit of fat suppression is the characterization of lesions containing macroscopic fat; such lesions will lose signal on fat-suppressed sequences as compared with the same sequence performed without fat suppression. Renal angiomyolipomas, adrenal myelolipomas, and retroperitoneal liposarcomas are examples of some of the more commonly encountered lesions in the urinary tract/retroperitoneum which contain macroscopic fat [67–69].

In- and Opposed-Phase (Chemical Shift) Imaging

This is a T1-weighted gradient echo sequence. Due to slight differences in their local chemical environment, water and fat protons will precess at slightly different frequencies. Over time, they will periodically resonate in phase and out of phase with each other at regular, predictable intervals, which is dependent on the magnetic field strength. This property is exploited with in- and opposed-phase imaging. Signal intensity on sequences obtained when water and fat protons are in phase with each other reflects the sum of the magnitude of water and fat signals. Conversely, opposed-phase imaging reflects the difference in magnitude of the opposed-phase water and fat vectors, as these vectors are opposed in direction and cancel each other out. Thus, tissues composed of 50 % fat and 50 % water will, in theory, have maximal signal loss (complete dropout) [67–69]. Conversely, tissues composed entirely or almost entirely of fat, such as some renal angiomyolipomas or adrenal myelolipomas, will have no change in signal as compared to the in-phase sequence (no dropout). Such lesions are best characterized on frequency-selective fat-suppressed sequences.

In- and opposed-phase imaging is routinely employed in urologic MR applications and plays a fundamental role in characterizing lesions containing microscopic fat. Examples of applications include fat detection in adrenal adenomas and clear-cell renal cell carcinoma. Opposed-phase images can be readily identified by a well-demarcated black line at any fat-water interface, the so-called India-ink artifact.

MR Urography

MR urography is an excellent method for noninvasive imaging of the urinary tract. Indications include evaluation of urinary tract obstruction, hematuria, congenital anomalies, and pre- and postsurgical anatomy. MR urography avoids the use of ionizing radiation and thus is of great benefit in evaluating pregnant patients and the pediatric population. MR urography is composed of two components: static-fluid MR urography and excretory MR urography.

In static-fluid MR urography, heavily T2-weighted sequences of the urinary tract are acquired, typically consisting of both high-resolution images and fast images acquired in rapid succession to create a cine series. Together, these can visualize the collecting systems, ureters, and bladder in their entirety. As visualization does not depend on excretion of contrast, static-fluid techniques are especially helpful in patients with dilated collecting systems and/or decreased renal function, in whom there may be poor contrast excretion and urinary tract opacification. Static-fluid techniques are also beneficial in subgroups of patients who are unable to receive intravenous contrast, including pregnancy, renal failure, and allergy.

Excretory MR urography, as its name implies, is performed in the excretory phase of contrast enhancement and can aid in the detection of mass lesions and assessment of renal function. Diuretic administration, usually low-dose furosemide, improves image quality in nondilated systems by enhancing urine flow, diluting the excreted contrast, and mildly distending the urinary tract.

Limitations of MR urography include long examination times, lower spatial resolution as compared with CT, and relative insensitivity to urinary tract calculi [72–74].

Basic Examination

The MRI exam begins with the patient being placed on a gantry which passes through the bore of the magnet. When exposed to a magnetic field, free water protons within atoms orient along the z-axis (head-to-toe axis) of the magnetic field. A radiofrequency coil is placed over the body part of interest. This typically consists of a coil which is placed outside the patient, positioned over the front and back of the patient; however, internal coils, such as endorectal coils, can be used for specific indications. The coil transmits the RF pulse through the patient. The effects of the RF pulse on the protons are expressed as a signal to obtain the magnetic

resonance image. Common generic sequences utilized in MR imaging of the GU tract include fast spin echo, single-shot fast spin echo with half-Fourier acquisition, 2D spoiled gradient echo, 3D spoiled gradient echo, and balanced steady-state gradient echo. Unfortunately, each MRI vendor has created unique trade names for these sequences, which often leads to undue confusion in trying to understand the properties, benefits, and limitations of each sequence [75].

Weighting of the image depends on TR and TE values as mentioned earlier in the general physics section. On T1-weighted images, fluid is low in signal, while on T2-weighted images, fluid is bright.

Relative and Absolute Contraindications

As there are many potential risks due to the strong magnetic field of MRI scanners, and previous adverse events and injuries have occurred involving patients, personnel, and equipment, the American College of Radiology recommends that all clinical and research MRI sites have a restricted zone, which includes the actual scanner room and an adjoining area, in which access is allowed only after careful MR safety screening. Any implantable device or potential foreign object must be carefully investigated for MR compatibility prior to the patient entering the restricted zone. These include, but are not limited to, vascular stents, stapes implant, implanted drug infusion device, neural growth stimulator, surgical clips, wire sutures, ocular prosthesis, joint replacement or prosthesis, bullets, and other foreign objects.

Contraindications to MRI include metal-containing implants which have the ability to heat or move when under the influence of a strong magnetic field or electronic implants which may be interrupted or permanently altered. These include pacemakers and defibrillators, metallic foreign body in the eye, deep brain stimulator, Swan-Ganz catheter, bullets or gunshot pellets, cerebral aneurysm clips, cochlear implants, magnetic dental implants, and drug infusion devices.

Other obstacles to MR examination include large patients that may be difficult to accommodate in the MRI bore, claustrophobic patients requiring sedation, significant pain limiting the patient's ability to lie still, and surgery in the previous 6 weeks [76].

Applications of MRI in the Urinary Tract

While CT is often the initial imaging modality for investigating genitourinary tract disease, advances in MRI, especially in terms of speed of image acquisition, have greatly improved the capabilities of MR imaging. MRI is superior to CT with regard to contrast resolution of soft tissue, often being able to further characterize equivocal CT or ultrasound findings.

MRI can frequently provide substantial information when iodinated contrast for CT cannot be administered, even in situations where contrast cannot be administered for the MR examination. One important limitation of MRI with regard to CT is inferior spatial resolution. Below we will explore the specific applications of MR imaging of the genitourinary tract by organ.

Kidney

CT is usually the first-line modality for renal mass evaluation; however, contrast-enhanced MRI has been shown to be a highly accurate modality for both detection and characterization of renal lesions [77, 78]. MRI is often useful for more definitive characterization of indeterminate lesions seen on CT. Weakly enhancing neoplasms such as papillary renal cell carcinoma may demonstrate equivocal levels of enhancement on CT [79–81]. Detection of enhancement within small (<1.5 cm) lesions is frequently confounded on CT due to pseudoenhancement artifact [30, 31]. Intralesional high attenuation within hemorrhagic cysts or tumors can make detection of enhancement difficult on CT. In all of these scenarios, MRI can provide more definitive evidence of enhancement and thus guide management [28, 77, 78, 82]. When evaluating cystic renal lesions, MRI can readily detect a proteinaceous or hemorrhagic cyst as a nonenhancing lesion with high T1 signal and can accurately evaluate the presence or absence of septal enhancement (Fig. 2.20) [28]. Calcifications within a complex cyst may cause artifact on CT, however calcifications do not interfere with the detection of enhancement on MRI. Therefore, MRI can more accurately detect enhancement within the wall of a complex cyst than will CT. Subtraction images, obtained by electronically subtracting the pre-contrast sequence from the post-contrast sequence, generate images composed exclusively of contrast signal and are useful in assessing enhancement (Fig. 2.21) [78, 82].

MRI can be used for staging renal cell carcinoma, with several studies showing similar accuracies of CT and MRI in staging based on the TNM system, including detection of renal vein and inferior vena cava invasion (Fig. 2.22) [83].

MRI is also useful in detecting fat within angiomyolipomas (AMLs). T1 fat-suppressed images are virtually diagnostic for AML if there is signal loss in the lesion when compared with a similar sequence performed without fat suppression (Fig. 2.23). 4–5 % of AMLs are lipid poor and either contain no fat or insufficient fat to be detected on imaging; these lesions cannot be reliably differentiated from renal cell cancer with any imaging modality [84]. Some AMLs may also lose signal (dropout) on opposed-phase imaging due to the presence of microscopic amounts
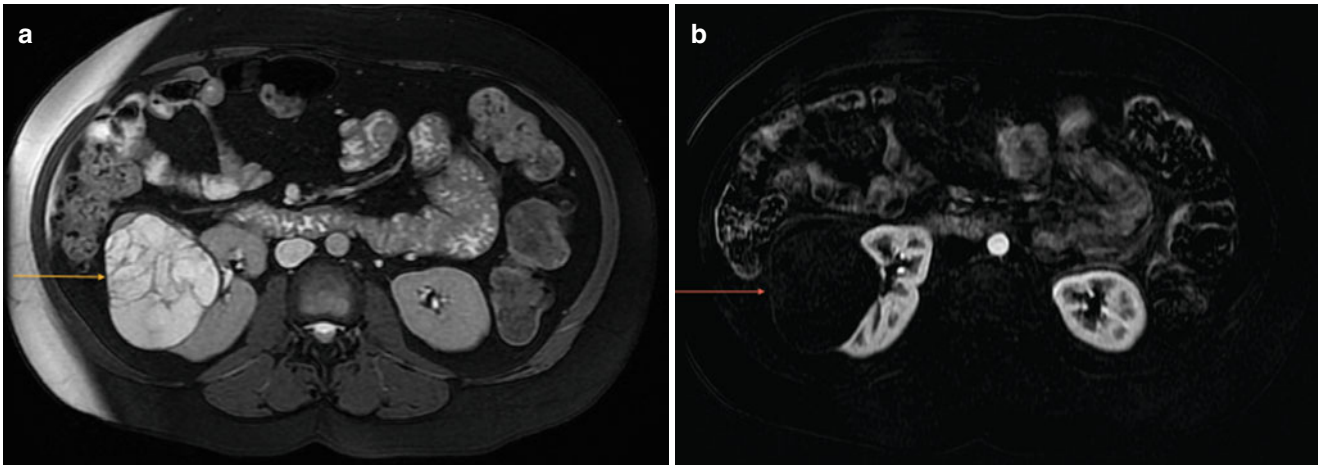
Fig. 2.20 Complex cystic renal mass. Axial T2-weighted (**a**) MRI image demonstrates a cystic right renal mass with numerous septations of varying thickness (*orange arrow* (**a**)). Contrast-enhanced subtraction image (**b**) shows the lack of enhancement within the wall of the mass or any of the septations (*arrow* (**b**)). The numerous septations in this mass raise suspicion for cystic renal cell carcinoma; however, the complete lack of enhancement suggests benignity: the septations may be sequelae of prior intracystic hemorrhage. This mass was stable for several years and thus likely benign
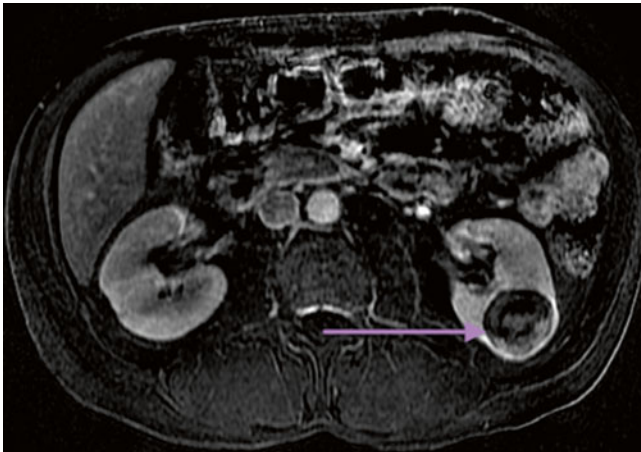

Fig. 2.21 Papillary renal cell carcinoma. Axial T1 post-contrast subtraction image at 100 s after contrast administration demonstrates mild heterogeneous enhancement of a left renal mass (*arrow*). Most papillary renal cell carcinomas demonstrate weak enhancement as compared with renal parenchyma. Subtraction images aid in evaluation of enhancement within a lesion. This finding was confirmed surgically

Fig. 2.22 Renal cell carcinoma with renal vein invasion. Axial "bright-blood" balanced gradient echo image demonstrates a large mass involving the left kidney (*yellow arrow*) with expansion of the left renal vein compatible with tumor thrombus (*purple arrow*). Note the difference in signal between the tumor-infiltrated left renal vein and the patent inferior vena cava. In patients who cannot receive intravenous contrast for MRI due to renal insufficiency, non-contrast imaging, including conventional, diffusion-weighted, gradient echo, and even MRA sequences, can often provide substantial information as compared to unenhanced CT scan

of fat within the tumor; however, caution should be exercised with this finding, as clear-cell renal cell carcinoma can also contain intracellular lipid and thus dropout on opposed-phase images (Fig. 2.24) [84, 85].

Adrenal

CT is the primary imaging modality for evaluating the adrenal glands; however, MRI plays a role in characterizing an adrenal mass in the setting of an equivocal CT and in patients who cannot receive iodinated contrast for CT. MRI is particularly useful in differentiating adrenal adenoma from metastasis.
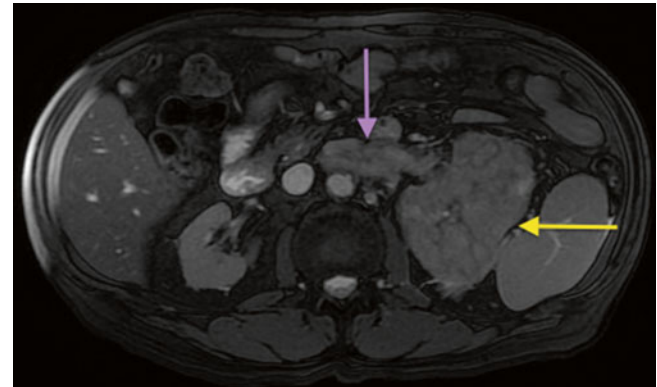
Adrenal metastases and adenomas are differentiated on the basis of chemical shift imaging. Adrenal adenomas contain intracellular lipid, whereas metastases do not. If the lesion in question demonstrates signal dropout on opposed-phase imaging, then it likely represents an adenoma (Fig. 2.25), except in rare instances, such as metastatic disease from a clear-cell renal cell carcinoma. Lesions with no change in signal on out-of-phase imaging either do not contain lipid or contain insufficient quantities of lipid to be detected on MRI and are thus indeterminate. Such a lesion could represent a lipid-poor
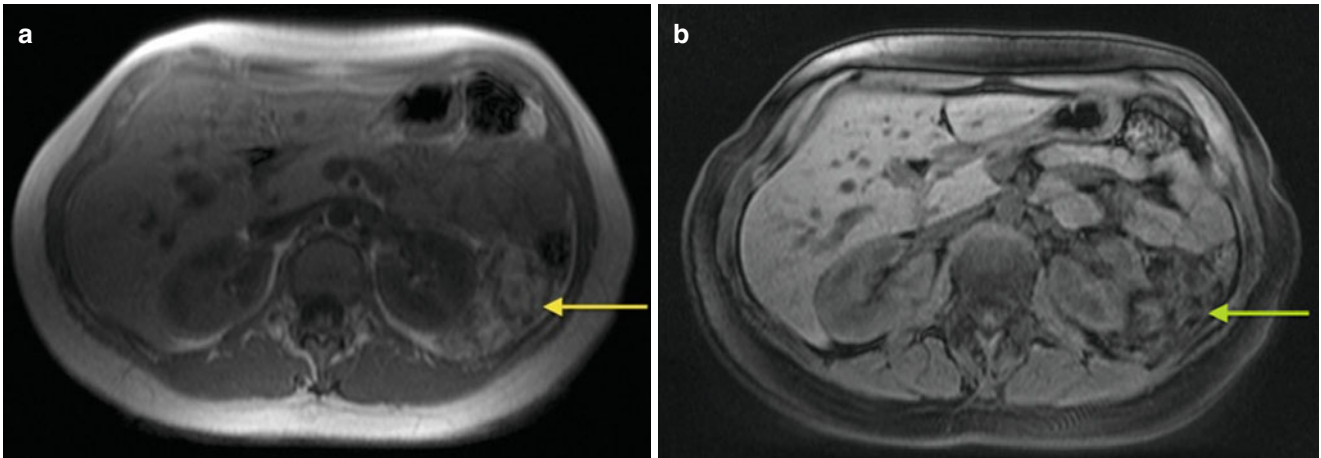
Fig. 2.23 Renal angiomyolipoma. Axial T1-weighted images obtained without (**a**) and with (**b**) fat suppression demonstrate a large, exophytic left renal mass (*arrows*) with areas of bulk fat which is bright on (**a**) and loses signal on the fat-suppressed image (**b**), compatible with an angiomyolipoma
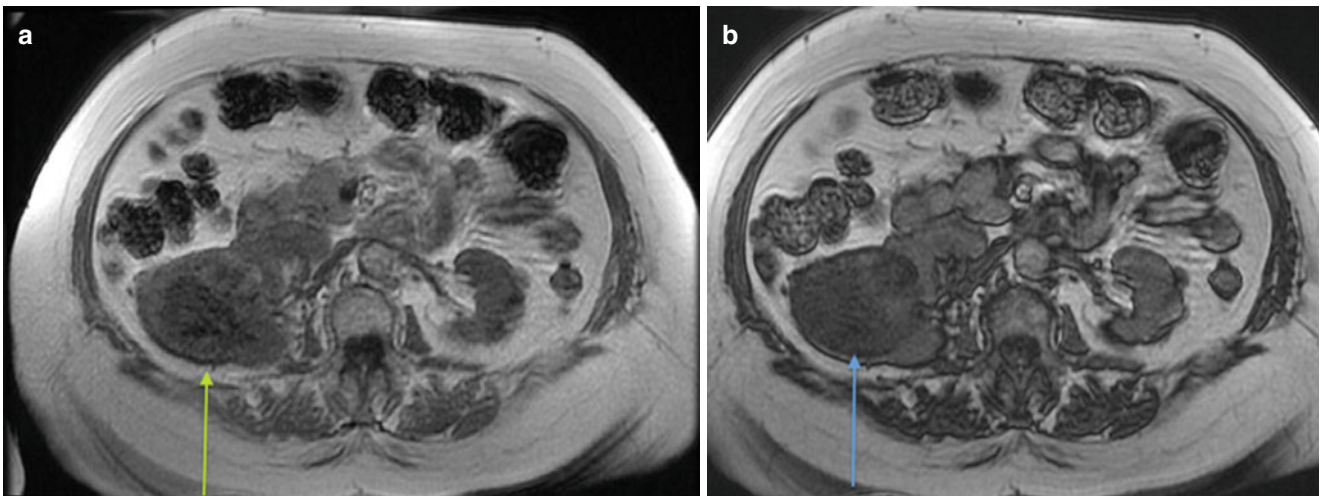

Fig. 2.24 Clear-cell renal cell carcinoma. Axial T1 in-phase (**a**) and opposed-phase (**b**) images demonstrate signal dropout within a large right renal mass (*arrows*) on opposed-phase imaging, confirming the presence of intracellular lipid. Dropout can also be seen in angiomyoli-pomas; however, in a lesion without macroscopic fat, this finding raises suspicion for clear-cell renal cell carcinoma, which was surgically confirmed
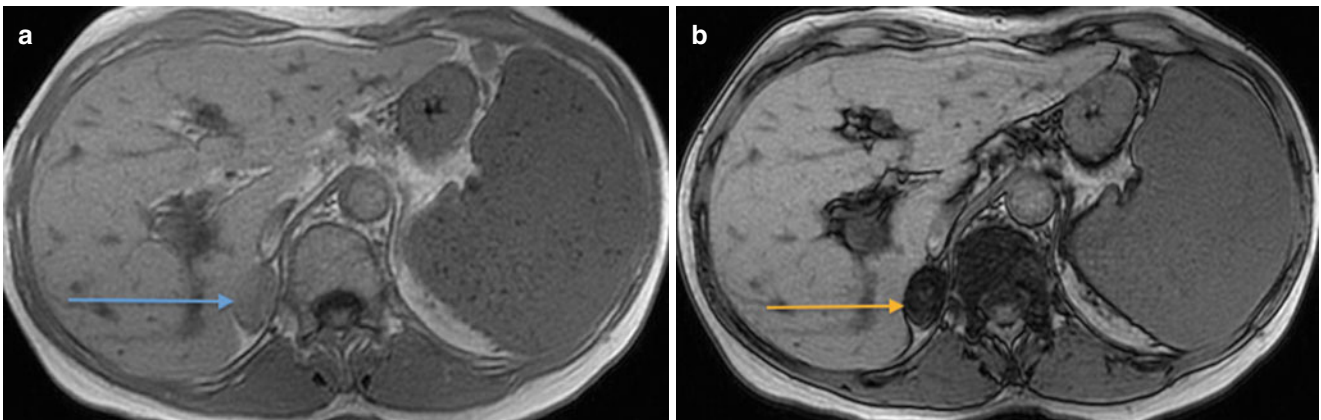

Fig. 2.25 Adrenal adenoma. Axial T1 in-phase (**a**) and opposed-phase (**b**) images demonstrate signal dropout of a right adrenal nodule (*arrows*) on opposed-phase imaging, confirming the presence of intracellular lipid and the diagnosis of an adrenal adenoma

adenoma or a non-adenomatous lesion. The sensitivity for adenoma detection with chemical shift imaging is approximately 80 % [86], which is similar to unenhanced CT.

Other adrenal lesions that can be specifically characterized by MRI include cyst and myelolipoma. However, the differential diagnosis of a non-cystic adrenal nodule devoid of fat is wide and must be correlated with a thorough biochemical and hormonal work-up for accurate diagnosis.

Approximately 65 % of pheochromocytomas are "lightbulb" bright on T2-weighted sequences; however, this is not a particularly sensitive or specific finding. A pheochromocytoma cannot be excluded on the basis of low T2 signal intensity, and other adrenal lesions, both benign and malignant, may have bright T2 signal [87, 88]. MRI, however, is an excellent modality for identifying extra-adrenal sites of pheochromocytoma, including the organ of Zuckerkandl, retroperitoneum, or carotid bulb.

Ureter and Bladder

MR urography is a useful method to evaluate the ureter and the bladder, especially in the pediatric age group and pregnant patients and in the setting of a contraindication to iodinated contrast. Congenital anomalies (Fig. 2.26), stenoses, obstruction, and filling defects due to stricture or neoplasm can be readily identified. MRI is significantly inferior to CT in the detection of ureteral calculi. The diagnosis of an obstructing ureteral stone on MRI is often made based on secondary findings, such as perirenal edema, ureteral dilatation, and perirenal fluid (Fig. 2.27) [72–74]. The role of MRI in bladder disease is not well established, although MRI has been used to detect tumors within diverticula, characterize intravesical pheochromocytoma, detect urachal tumors, and stage bladder cancer [89].
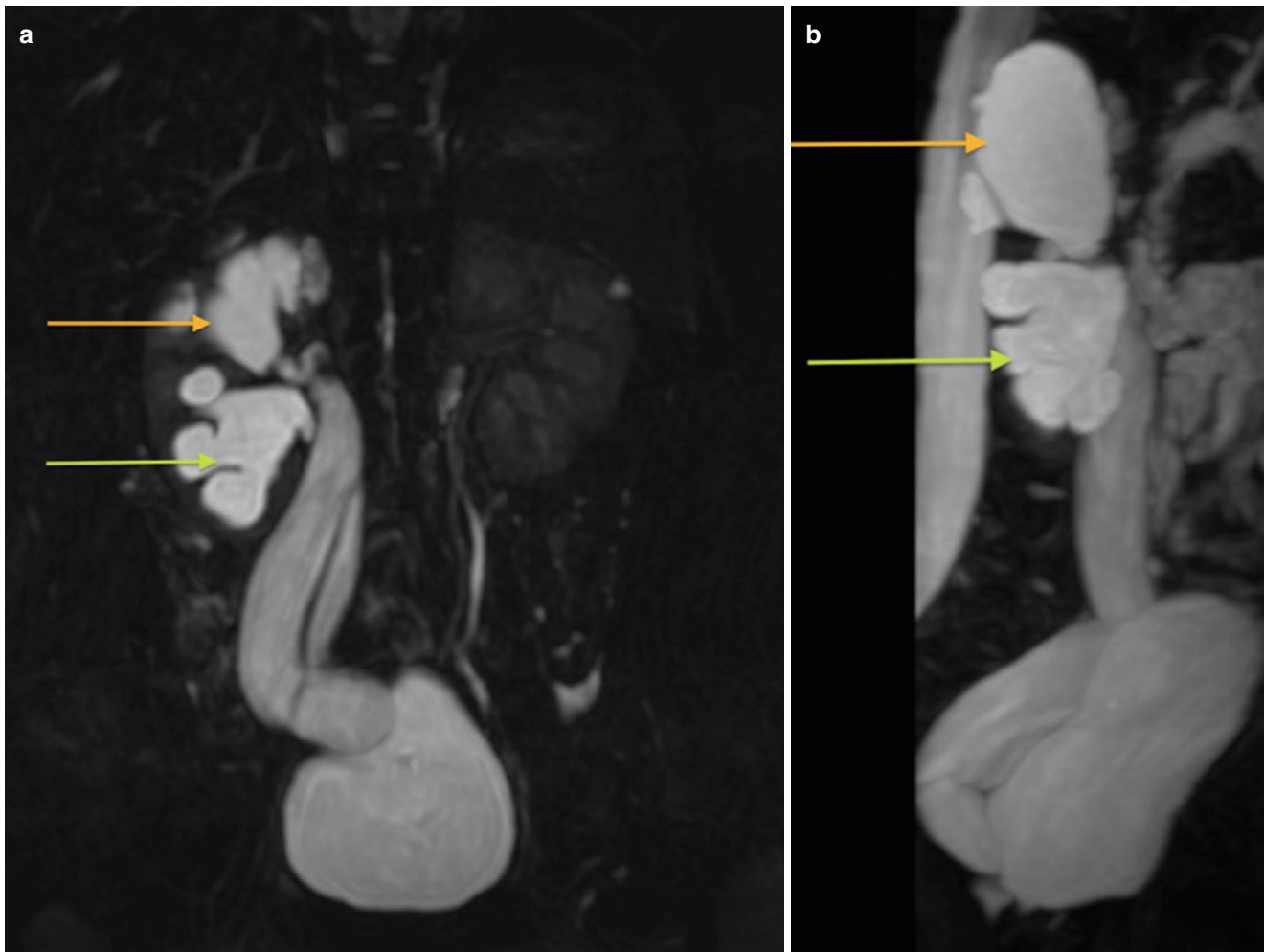
Fig. 2.26 Congenital duplicated renal collecting system with obstruction. Coronal (**a**) and sagittal (**b**) heavily T2-weighted images from an MR urogram demonstrate a right duplex collecting system with obstruction of the upper pole collecting moiety (*orange arrow*) and a low ectopic insertion of the ureter draining the upper pole (**b**). There is also dilatation of the lower pole collecting system (*green arrows*), possibly due to reflux
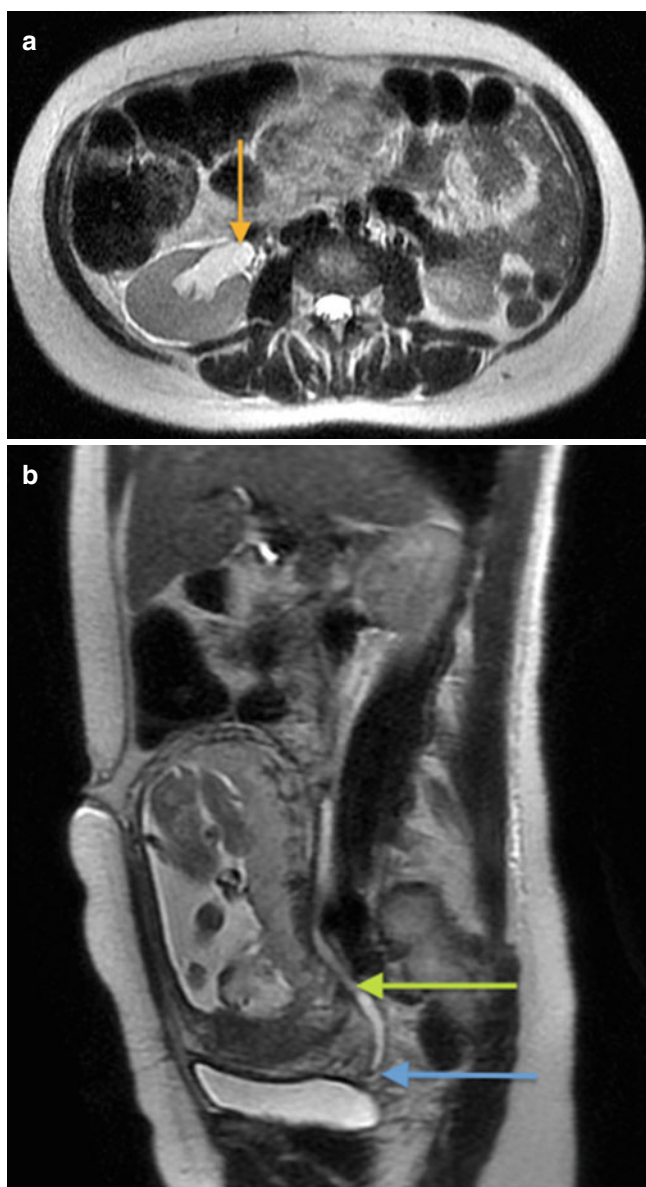
Fig. 2.27 Obstructing right ureteral calculus in a pregnant patient. Axial (**a**) and sagittal (**b**) T2-weighted images demonstrate mild right hydronephrosis (*orange arrow*) and hydroureter (*green arrow*) secondary to a low-signal distal right ureteral calculus (*blue arrow*). A gravid uterus is noted. In hydronephrosis of pregnancy, the ureter usually shows gradual tapering at the level of the pelvic brim, as opposed to this example, where the ureter remains dilated down to the ureterovesical junction

Prostate

MRI of the prostate offers accurate detection and local staging of prostate cancer. The advent of high-strength (3 T) magnetic fields and endorectal surface coils has led to signal to noise ratio increases, providing higher-resolution imaging of the prostatic surface and internal anatomy. A complete MRI exam of the prostate should include conventional T1- and T2-weighted spin-echo sequences, DWI with correlative ADC maps, and dynamic contrast-enhanced sequences. Prostate cancer typically appears as a region of hypointense T2 signal. The majority of cancers are located in the normally T2-hyperintense peripheral zone and often demonstrate diffusion restriction. Approximately 30 % of cancers occur in the central zone. Detection of these cancers may be more problematic due to the frequent presence of hyperplasia, resulting in a background of heterogeneous T2 signal and enhancement.

DWI now plays an important role in prostate cancer detection on MRI [90–92]. The use of high B values (1000 or greater) may increase sensitivity and specificity for lesion detection (Fig. 2.28) [93].

Contrast-enhanced imaging is typically performed with repeated ultrafast acquisitions after contrast injection, which provide high temporal resolution and the ability to assess contrast enhancement as a function of time. Prostate cancer generally demonstrates earlier and higher peak enhancement and early washout as compared with normal prostatic tissue [93].

MR spectroscopy is a technique which can separate out compounds in tissue based on their Larmor frequency (see discussion above). Citrate is found in relatively high concentrations in normal prostate and decreased amounts in prostate cancer (and other conditions such as prostatitis and hemorrhage). Choline can be detected on MRI spectroscopy as an aggregate peak of choline-containing cell membrane compounds. Choline is found in high amounts in prostate cancer due to rapid cell membrane turnover and relatively increased cell surface ratio. Increased choline concentration is the hallmark of prostate cancer, although it can be found in benign conditions such as prostatitis [93].

MRI is the most accurate imaging modality for differentiating between organ-confined (T1 or T2) and extracapsular (T3) diseases, although there are a wide range of sensitivities and specificities reported in the literature [93].

MRI is also playing a larger role in obtaining tissue diagnosis of prostate cancer. MR images can be coregistered with real-time ultrasound (US) imaging (MRI/US fusion biopsy), providing a target for US-guided biopsy. This has been shown to increase cancer detection rates compared with traditional transrectal US-guided biopsy, which is typically performed in blind fashion, by obtaining 12 core samples, without visualization of a target lesion. MRI/US fusion biopsy appears to be especially suited for patients with high suspicion for prostate cancer and negative US-guided biopsy [94].
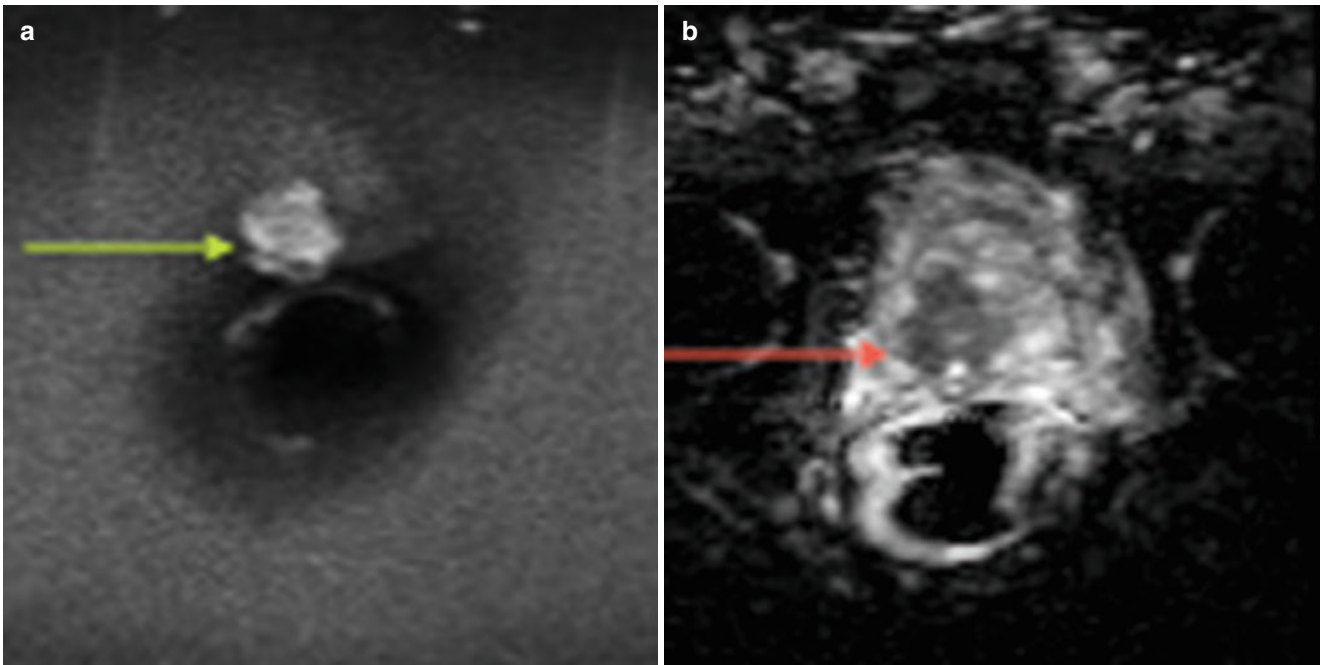
Fig. 2.28 Prostate cancer. b2000 diffusion-weighted image (**a**) and corresponding ADC map (**b**) demonstrate a large region of diffusion restriction within the peripheral zone of the prostate on the right, manifested by high signal on the diffusion image (*green arrow*, (**a**)) and low signal on the ADC map (*red arrow* (**b**)). Such markedly restricted diffusion is a highly suspicious finding for malignancy

Scrotum

Ultrasound is the primary imaging modality for the evaluation of the scrotum and testicles. MRI evaluation of the scrotum is limited by long examination times and lack of portability and availability, especially after hours. On MR, normal testes have homogeneous intermediate intensity on T1-weighted images and high signal on T2-weighted images. The testicles are surrounded by the fibrous tunica albuginea, which is low in signal intensity on T2-weighted images. The role of MRI in imaging the scrotum often revolves around adding additional information in cases where ultrasound findings are equivocal. For example, MRI can help define the pattern of injury in the setting of testicular trauma. An area of heterogeneous signal intensity on T2-weighted images should raise the possibility of testicular injury. Disruption in the normal low-signal tunica albuginea is diagnostic of testicular rupture; therefore, the tunica should be carefully assessed in all three planes [16, 95]. Another emerging application for scrotal MRI is in the differentiation of segmental testicular infarction versus small neoplasm. An avascular area on contrast-enhanced images with an enhancing rim is typically seen with infarction [16, 96]. Although not typically used in diagnosing and staging testicular cancer, MRI has been shown to be quite sensitive and specific in detecting testicular tumors, differentiating benign from malignant lesions (Fig. 2.29), and diagnosing local invasion [97].

Penis

Ultrasound is the primary modality in the evaluation of penile disease; however, MRI does have a role in the evaluation of blunt penile trauma. MR is able to depict the fascial layers of the penis in exquisite detail, demonstrating the presence and site of disruption of the normal low-signal tunica albuginea surrounding the corpus cavernosa (Fig. 2.30) and directing surgical repair [16, 98–100]. Other potential applications of MRI in evaluating penile disease include cancer staging, mass characterization, detection of plaques in Peyronie's disease, and localization of periurethral abscesses [16, 100].

Female Urethra

MRI plays a significant role in the diagnosis of urethral and periurethral disease in women, particularly in the evaluation of ureteral diverticula. The examination can be performed with a torso phased-array coil or an endoluminal coil
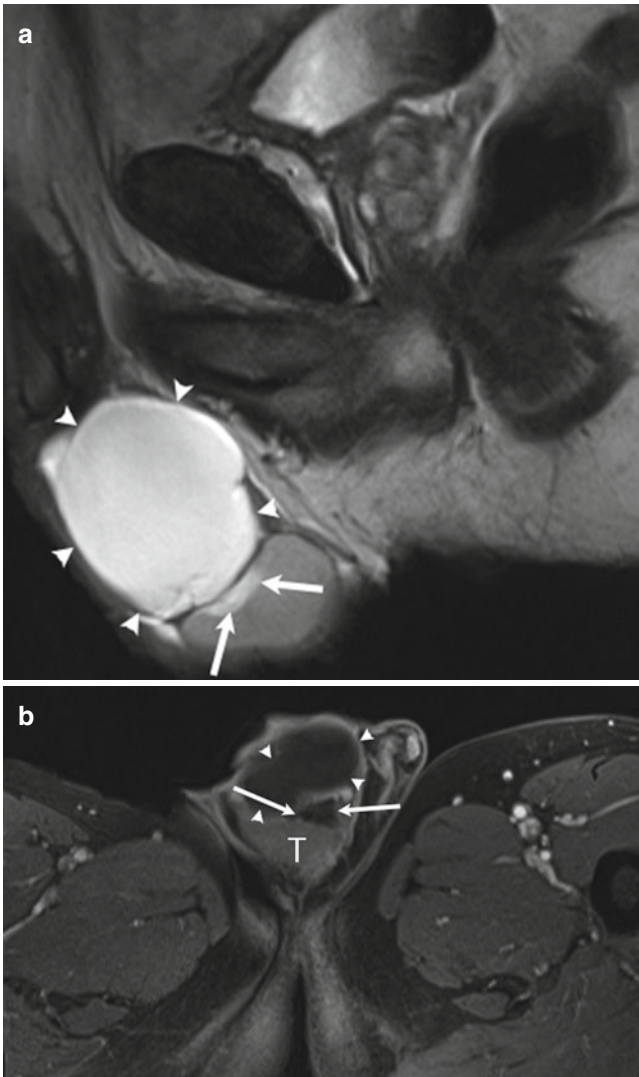
Fig. 2.29 Epididymal head cyst and dilatation of the rete testes. Sagittal T2-weighted (**a**) and axial T1-weighted gadolinium-enhanced images (**b**) demonstrate a large mass (*arrowheads*) above the right testicle ("T" in (**b**)). This is uniformly hyperintense on the T2-weighted and does not enhance, compatible with an epididymal head cyst. The patient had been referred to MRI for the evaluation of an indeterminate testicular lesion seen on ultrasound. The lesion (*arrows*) is bright on the T2-weighted sequence and does not enhance, compatible with a benign lesion, most likely dilatation of the rete testes

Fig. 2.30 Coronal (**a**) and sagittal (**b**) T2-weighted, fat-saturated MRI sequences demonstrate a mixed-signal collection inferior to the penile shaft (*orange arrow* in (**a**), *purple arrow* in (**b**)) compatible with a hematoma. The low-signal tunica albuginea is well visualized and is intact (*red arrow* in (**a**), *green arrow* in (**b**))

(endovaginal, endorectal, endourethral) to improve resolution and signal to noise ratio. Normally, on T2-weighted images, the urethral mucosa and muscle are hypointense, while the submucosa is hyperintense. A urethral diverticulum can be identified as single or multiple, unilocular, or multilocular on T2-weighted images. Circumferential involvement of t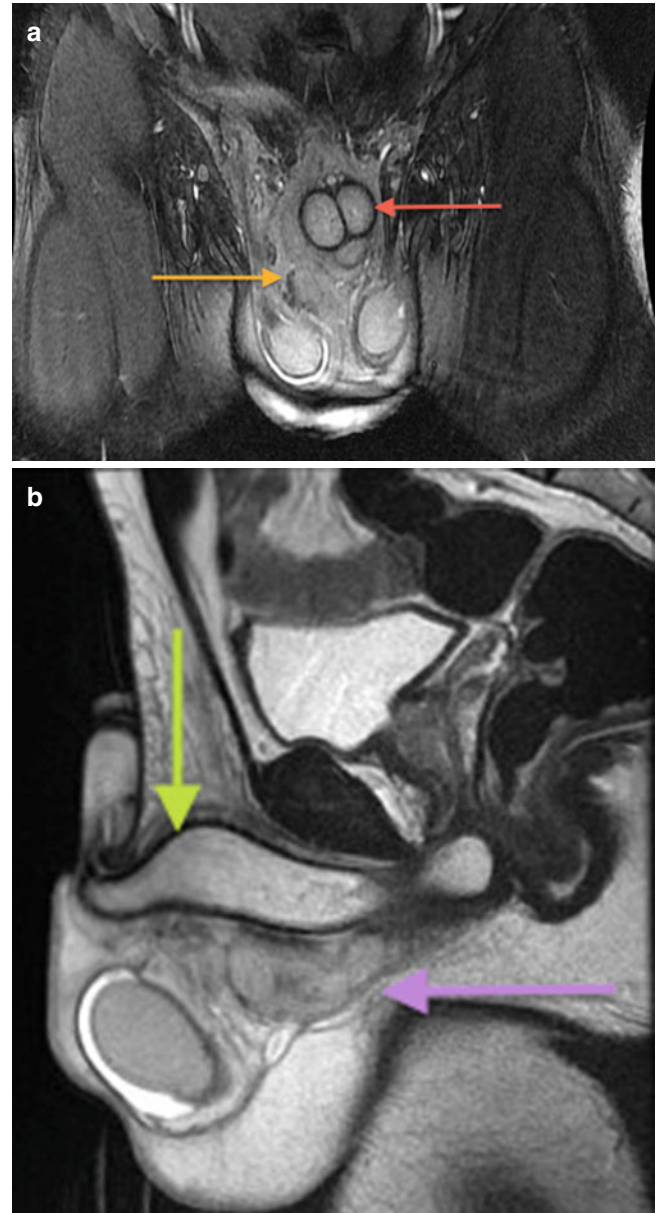he urethra, in a "saddle bag" configuration, is a common appearance of a urethral diverticulum. Post-contrast administration aids in the detection of diverticular inflammation or adenocarcinoma, depicted as a small enhancing soft tissue mass within the diverticulum. MRI is more sensitive than urethrography and urethroscopy for the diagnosis of urethral diverticulum and is indicated when clinical suspicion is strong and other modalities are inconclusive [101].

References

1. Bushberg JT, Boone JM. The essential physics of medical imaging. Philadelphia: Lippincott Williams & Wilkins; 2011.

2. Resnick MI, Spirnak JP. Basic principles of ultrasound. In: Gillenwater JY, editor. Adult and pediatric urology, vol. 1. Philadelphia: Lippincott Williams & Wilkins; 2002.

3. Scherzinger AL, Stamm E. Ultrasound-concepts and transducers. In: RSNA/AAPM Physics Modules members-only website. Retrieved from http://www.rsna.org/RSNA/AAPM_Online_Physics_Modules_.aspx.

4. Feldman MK, Katyal S, Blackwood MS. US artifacts 1. Radiographics. 2009;29(4):1179–89.

5. Badler R, Bordia R, Venkataramanan N. Interaction of ultrasound tissue and Doppler. In: RSNA/AAPM Physics Modules members-only website. Retrieved from http://www.rsna.org/RSNA/AAPM_Online_Physics_Modules_.aspx.

6. Evans KD, Layman R, Volz K. Image quality-artifacts-doppler-safety. In: RSNA/AAPM Physics Modules members-only website. Retrieved from http://www.rsna.org/RSNA/AAPM_Online_Physics_Modules_.aspx.

7. Merritt CR. Doppler US: the basics. Radiographics. 1991;11(1):109–19.

8. Daneman A, Navarro OM, Somers GR, Mohanta A, Jarrín JR, Traubici J. Renal pyramids: focused sonography of normal and pathologic processes 1. Radiographics. 2010;30(5):1287–307.

9. Hartman DS, Choyke PL, Hartman MS. From the RSNA refresher courses: a practical approach to the cystic renal mass 1. Radiographics. 2004;24 Suppl 1:S101–15.

10. Wagner BJ, Wong-You-Cheong JJ, Davis Jr CJ. Adult renal hamartomas. Radiographics. 1997;17(1):155–69.

11. Brown ED, Chen MY, Wolfman NT, Ott DJ, Watson Jr NE. Complications of renal transplantation: evaluation with US and radionuclide imaging 1. Radiographics. 2000;20(3):607–22.

12. Yacoub JH, Verma S, Moulton JS, Eggener S, Oto A. Imaging-guided prostate biopsy: conventional and emerging techniques. Radiographics. 2012;32(3):819–37.

13. Hernandez J, Thompson IM. Carcinoma core distribution in patients with palpable and nonpalpable prostate tumors. Cancer. 2005;103(9):1761–2.

14. Tamsel S, Killi R, Hekimgil M, Altay B, Soydan S, Demirpolat G. Transrectal ultrasound in detecting prostate cancer compared with serum total prostate-specific antigen levels. J Med Imaging Radiat Oncol. 2008;52(1):24–8.

15. Zisman A, Herbert M, Strauss S, Manor H, Liebovici D, Lindner A. Preoperative detection of locally advanced prostate cancer by using transrectal ultrasound-guided staging prostate biopsy. The Prostate J. 2000;2(3):130–6.

16. Avery LL, Scheinfeld MH. Imaging of penile and scrotal emergencies. Radiographics. 2013;33(3):721–40.

17. Aso C, Enríquez G, Fité M, Torán N, Piró C, Piqueras J, Lucaya J. Gray-scale and color Doppler sonography of scrotal disorders in children: an update 1. Radiographics. 2005;25(5):1197–214.

18. Pauroso S, Di Leo N, Fulle I, Di Segni M, Alessi S, Maggini E. Varicocele: ultrasonographic assessment in daily clinical practice. J Ultrasound. 2011;14(4):199–204.

19. Mahesh M. The AAPM/RSNA physics tutorial for residents: search for isotropic resolution in CT fr from conventional through multiple-Row detector. Radiographics. 2002;22(4):949–62.

20. Hartman R, Kawashima A, Takahashi N, Silva A, Vrtiska T, Leng S, Fletcher J, McCollough C. Applications of dual-energy CT in urologic imaging: an update. Radiol Clin North Am. 2012;50(2):191–205.

21. Song KD, Kim CK, Park BK, Kim B. Utility of iodine overlay technique and virtual unenhanced images for the characterization of renal masses by dual-energy CT. Am J Roentgenol. 2011;197(6):W1076–82.

22. Neville AM, Gupta RT, Miller CM, Merkle EM, Paulson EK, Boll DT. Detection of renal lesion enhancement with dual-energy multidetector CT. Radiology. 2011;259(1):173–83.

23. Graser A, Johnson TR, Hecht EM, Becker CR, Leidecker C, Staehler M, Stief CG, Hildebrandt H, Godoy MC, Finn ME, Stepansky F, Reiser MF, Macari M. Dual-energy CT in patients suspected of having renal masses: can virtual nonenhanced images replace true nonenhanced images? Radiology. 2009;252(2):433–40.

24. Gnannt R, Fischer M, Goetti R, Karlo C, Leschka S, Alkadhi H. Dual-energy CT for characterization of the incidental adrenal mass: preliminary observations. Am J Roentgenol. 2012;198(1):138–44.

25. Gupta RT, Ho LM, Marin D, Boll DT, Barnhart HX, Nelson RC. Dual-energy CT for characterization of adrenal nodules: initial experience. Am J Roentgenol. 2010;194(6):1479–83.

26. Boll DT, Patil NA, Paulson EK, Merkle EM, Simmons WN, Pierre SA, Preminger GM. Renal stone assessment with dual-energy multidetector CT and advanced postprocessing techniques: improved characterization of renal stone composition—pilot study 1. Radiology. 2009;250(3):813–20.

27. Zilberman DE, Ferrandino MN, Preminger GM, Paulson EK, Lipkin ME, Boll DT. In vivo determination of urinary stone composition using dual energy computerized tomography with advanced post-acquisition processing. J Urol. 2010;184(6):2354–9.

28. Israel GM, Bosniak MA. How i do it: evaluating renal masses. Radiology. 2005;236(2):441–50.

29. Taneja R, Bhargava P, Cuevas C, Dighe MK. Common and less-common renal masses and masslike conditions. Radiol Clin North Am. 2012;50(2):245–57.

30. Birnbaum BA, Maki DD, Chakraborty DP, Jacobs JE, Babb JS. Renal cyst pseudoenhancement: evaluation with an anthropomorphic body CT phantom. Radiology. 2002;225(1):83–90.

31. Wang ZJ, Coakley FV, Fu Y, Joe BN, Prevrhal S, Landeras LA, Webb EM, Yeh BM. Renal cyst pseudoenhancement at multidetector CT: what Are the effects of number of detectors and peak tube voltage? Radiology. 2008;248(3):910–6.

32. Ng CS, Wood CG, Silverman PM, Tannir NM, Tamboli P, Sandler CM. Renal cell carcinoma: diagnosis, staging, and surveillance. Am J Roentgenol. 2008;191(4):1220–32.

33. Johnson CD, Dunnick NR, Cohan RH, Illescas FF. Renal adenocarcinoma: CT staging of 100 tumors. Am J Roentgenol. 1987;148(1):59–63.

34. Hammond NA, Nikolaidis P, Miller FH. Infectious and inflammatory diseases of the kidney. Radiol Clin North Am. 2012;50(2):259–70.

35. Stunell H, Buckley O, Feeney J, Geoghegan T, Browne RFJ, Torreggiani WC. Imaging of acute pyelonephritis in the adult. Eur Radiol. 2007;17(7):1820–8.

36. Santucci RA, Wessells H, Bartsch G, Descotes J, Heyns CF, McAninch JW, Nash P, Schmidlin F. Evaluation and management of renal injuries: consensus statement of the renal trauma subcommittee. BJU Int. 2004;93(7):937–54.

37. Moore EE, Shackford SR, Pachter HL, McAninch JW, Browner BD, Champion HR, Flint LM, Gennarelli TA, Malangoni MA, Ramenofsky ML, Trafton PG. Organ injury scaling: spleen, liver, and kidney. J Trauma. 1989;29(12):1664–6.

38. Lee YJ, Oh SN, Rha SE, Byun JY. Renal trauma. Radiol Clin North Am. 2007;45(3):581–92.

39. Boulay I, Holtz P, Foley WD, White B, Begun FP. Ureteral calculi: diagnostic efficacy of helical CT and implications for treatment of patients. AJR Am J Roentgenol. 1999;172(6):1485–90.

40. Hamm M, Wawroschek F, Weckermann D, Knöpfle E, Häckel T, Häuser H, Krawczak G, Harzmann R. Unenhanced helical computed tomography in the evaluation of acute flank pain. Eur Urol. 2001;39(4):460–5.

41. Fielding JR, Fox LA, Heller H, Seltzer SE, Tempany CM, Silverman SG, Steele G. Spiral CT in the evaluation of flank pain: overall accuracy and feature analysis. J Comput Assist Tomogr. 1997;21(4):635–8.

42. Katz DS, Lane MJ, Sommer FG. Unenhanced helical CT of ureteral stones: incidence of associated urinary tract findings. AJR Am J Roentgenol. 1996;166(6):1319–22.

43. Kambadakone AR, Eisner BH, Catalano OA, Sahani DV. New and evolving concepts in the imaging and management of urolithiasis: urologists' perspective. Radiographics. 2010;30(3):603–23.

44. Berland LL, Silverman SG, Gore RM, Mayo-Smith WW, Megibow AJ, Yee J, Brink JA, Baker ME, Federle MP, Foley WD, Francis IR, Herts BR, Israel GM, Krinsky G, Platt JF, Shuman WP, Taylor AJ. Managing incidental findings on abdominal CT: white paper of the ACR incidental findings committee. J Am Coll Radiol. 2010;7(10):754–73.

45. Young Jr WF. The incidentally discovered adrenal mass. N Eng J Med. 2007;356(6):601–10.

46. Taffel M, Haji-Momenian S, Nikolaidis P, Miller FH. Adrenal imaging: a comprehensive review. Radiol Clin North Am. 2012; 50(2):219–43.

47. Boland GW, Lee M, Gazelle GS, Halpern EF, McNicholas MM, Mueller PR. Characterization of adrenal masses using unenhanced CT: an analysis of the CT literature. AJR Am J Roentgenol. 1998;171(1):201–4.

48. Caoili EM, Korobkin M, Francis IR, Cohan RH, Platt JF, Dunnick NR, Raghupathi KI. Adrenal masses: characterization with combined unenhanced and delayed enhanced CT. Radiology. 2002;222(3):629–33.

49. Johnson PT, Horton KM, Fishman EK. Adrenal imaging with multidetector CT: evidence-based protocol optimization and interpretative practice 1. Radiographics. 2009;29(5):1319–31.

50. Raisanen J, Shapiro B, Glazer GM, Desai S, Sisson JC. Plasma catecholamines in pheochromocytoma: effect of urographic contrast media. Am J Roentgenol. 1984;143(1):43–6.

51. Mukherjee JJ, Peppercorn PD, Reznek RH, Patel V, Kaltsas G, Besser M, Grossman AB. Pheochromocytoma: effect of nonionic contrast medium in CT on circulating catecholamine levels. Radiology. 1997;202(1):227–31.

52. Bessell-Browne R, O'Malley ME. CT of pheochromocytoma and paraganglioma: risk of adverse events with iv administration of nonionic contrast material. Am J Roentgenol. 2007;188(4):970–4.

53. Mezhir JJ, Song J, Piano G, Testa G, Raman J, Al-Ahmadie HA, Angelos P. Adrenocortical carcinoma invading the inferior vena cava: case report and literature review. Endocr Pract. 2008;14(6):721–5.

54. Bhargava P, Dighe MK, Lee JH, Wang C. Multimodality imaging of ureteric disease. Radiol Clin North Am. 2012;50(2):271–99.

55. Chow LC, Kwan SW, Olcott EW, Sommer G. Split-bolus MDCT urography with synchronous nephrographic and excretory phase enhancement. Am J Roentgenol. 2007;189(2):314–22.

56. Chlapoutakis K, Theocharopoulos N, Yarmenitis S, Damilakis J. Performance of computed tomographic urography in diagnosis of upper urinary tract urothelial carcinoma, in patients presenting with hematuria: systematic review and meta-analysis. Eur J Radiol. 2010;73(2):334–8.

57. Mouli S, Casalino DD, Nikolaidis P. Imaging features of common and uncommon bladder neoplasms. Radiol Clin North Am. 2012;50(2):301–16.

58. Knox MK, Cowan NC, Rivers-Bowerman MD, Turney BW. Evaluation of multidetector computed tomography urography and ultrasonography for diagnosing bladder cancer. Clin Radiol. 2008;63(12):1317–25.

59. Sadow CA, Silverman SG, O'Leary MP, Signorovitch JE. Bladder cancer detection with CT urography in an academic medical center. Radiology. 2008;249(1):195–202.

60. Vikram R, Sandler CM, Ng CS. Imaging and staging of transitional cell carcinoma: part 1, lower urinary tract. Am J Roentgenol. 2009;192(6):1481–7.

61. Chan DP, Abujudeh HH, Cushing Jr GL, Novelline RA. CT cystography with multiplanar reformation for suspected bladder rupture: experience in 234 cases. Am J Roentgenol. 2006;187(5):1296–302.

62. Quagliano PV, Delair SM, Malhotra AK. Diagnosis of blunt bladder injury: a prospective comparative study of computed tomography cystography and conventional retrograde cystography. J Trauma Acute Care Surg. 2006;61(2):410–22.

63. Balter S. An introduction to the physics of magnetic resonance imaging. Radiographics. 1987;7(2):371–83.

64. Pooley RA. Fundamental physics of MR imaging. Radiographics. 2005;25(4):1087–99.

65. Plewes DB. The AAPM/RSNA physics tutorial for residents. Contrast mechanisms in spin-echo MR imaging. Radiographics. 1994;14(6):1389–404.

66. Price RR. The AAPM/RSNA physics tutorial for residents. Contrast mechanisms in gradient-echo imaging and an introduction to fast imaging. Radiographics. 1995;15(1):165–78.

67. Bley TA, Wieben O, François CJ, Brittain JH, Reeder SB. Fat and water magnetic resonance imaging. J Magn Reson Imaging. 2010; 31(1):4–18.

68. Pokharel SS, Macura KJ, Kamel IR, Zaheer A. Current MR imaging lipid detection techniques for diagnosis of lesions in the abdomen and pelvis. Radiographics. 2013;33(3):681–702.

69. Delfaut EM, Beltran J, Johnson G, Rousseau J, Marchandise X, Cotten A. Fat suppression in MR imaging: techniques and pitfalls. Radiographics. 1999;19(2):373–82.

70. Qayyum A. Diffusion-weighted imaging in the abdomen and pelvis: concepts and applications. Radiographics. 2009;29(6): 1797–810.

71. Neil JJ. Measurement of water motion (apparent diffusion) in biological systems. Concepts Magn Reson. 1997;9(6):385–401.

72. Leyendecker JR, Barnes CE, Zagoria RJ. MR urography: techniques and clinical applications. Radiographics. 2008;28(1): 23–46.

73. Nolte-Ernsting CCA, Staatz G, Tacke J, Günther RW. MR urography today. Abdom Imaging. 2003;28(2):0191–209.

74. Leyendecker JR, Gianini JW. Magnetic resonance urography. Abdom Imaging. 2009;34(4):527–40.

75. Lin E. Body MRI sequences: a conceptual framework. Appl Radiol. 2012;41(1):16–23.

76. Kanal E, Barkovich AJ, Bell C, Borgstede JP, Bradley WG, Froelich JW, Gimbel JR, Gosbee JW, Kuhni-Kaminski E, Larson PA, Lester Jr JW, Nyenhuis J, Schaefer DJ, Sebek EA, Weinreb J, Wilkoff BL, Woods TO, Lucey L, Hernandez D. ACR guidance document on MR safe practices: 2013. J Magn Reson Imaging. 2013;37(3): 501–30.

77. Ho VB, Allen SF, Hood MN, Choyke PL. Renal masses: quantitative assessment of enhancement with dynamic MR imaging. Radiology. 2002;224(3):695–700.

78. Hecht EM, Israel GM, Krinsky GA, Hahn WY, Kim DC, Belitskaya-Levy I, Lee VS. Renal masses: quantitative analysis of enhancement with signal intensity measurements versus qualitative analysis of enhancement with image subtraction for diagnosing malignancy at MR imaging. Radiology. 2004;232(2):373–8.

79. Herts BR, Coll DM, Novick AC, Obuchowski N, Linnell G, Wirth SL, Baker ME. Enhancement characteristics of papillary renal neoplasms revealed on triphasic helical CT of the kidneys. Am J Roentgenol. 2002;178(2):367–72.

80. Roy C, Sauer B, Lindner V, Lang H, Saussine C, Jacqmin D. MR imaging of papillary renal neoplasms: potential application for characterization of small renal masses. Eur Radiol. 2007;17(1): 193–200.

81. Sun MR, Ngo L, Genega EM, Atkins MB, Finn ME, Rofsky NM, Pedrosa I. Renal cell carcinoma: dynamic contrast-enhanced MR imaging for differentiation of tumor subtypes—correlation with pathologic findings. Radiology. 2009;250(3):793–802.

82. Newatia A, Khatri G, Friedman B, Hines J. Subtraction imaging: applications for nonvascular abdominal MRI. Am J Roentgenol. 2007;188(4):1018–25.

83. Nikken JJ, Krestin GP. MRI of the kidney—state of the art. Eur Radiol. 2007;17(11):2780–93.

84. Silverman SG, Mortele KJ, Tuncali K, Jinzaki M, Cibas ES. Hyperattenuating renal masses: etiologies, pathogenesis, and imaging evaluation. Radiographics. 2007;27(4):1131–43.

85. Outwater EK, Bhatia M, Siegelman ES, Burke MA, Mitchell DG. Lipid in renal clear cell carcinoma: detection on opposed-phase gradient-echo MR images. Radiology. 1997;205(1): 103–7.

86. Outwater EK, Siegelman ES, Radecki PD, Piccoli CW, Mitchell DG. Distinction between benign and malignant adrenal masses: value of T1-weighted chemical-shift MR imaging. AJR Am J Roentgenol. 1995;165(3):579–83.

87. Varghese JC, Hahn PF, Papanicolaou N, Mayo-Smith WW, Gaa JA, Lee MJ. MR differentiation of phaeochromocytoma from other adrenal lesions based on qualitative analysis of T2 relaxation times. Clin Radiol. 1997;52(8):603–6.

88. Blake MA, Kalra MK, Maher MM, Sahani DV, Sweeney AT, Mueller PR, Hahn PF, Boland GW. Pheochromocytoma: an imaging chameleon. Radiographics. 2004;24 Suppl 1:S87–99.

89. Tekes A, Kamel I, Imam K, Szarf G, Schoenberg M, Nasir K, Thompson R, Bluemke D. Dynamic MRI of bladder cancer: evaluation of staging accuracy. Am J Roentgenol. 2005;184(1):121–7.

90. Haider MA, van der Kwast TH, Tanguay J, Evans AJ, Hashmi AT, Lockwood G, Trachtenberg J. Combined T2-weighted and diffusion-weighted MRI for localization of prostate cancer. Am J Roentgenol. 2007;189(2):323–8.

91. Tamada T, Sone T, Jo Y, Toshimitsu S, Yamashita T, Yamamoto A, Tanimoto D, Ito K. Apparent diffusion coefficient values in peripheral and transition zones of the prostate: comparison between normal and malignant prostatic tissues and correlation with histologic grade. J Magn Reson Imaging. 2008;28(3): 720–6.

92. Katahira K, Takahara T, Kwee TC, Oda S, Suzuki Y, Morishita S, Kitani K, Hamada Y, Kitaoka M, Yamashita Y. Ultra-high-b-value diffusion-weighted MR imaging for the detection of prostate cancer: evaluation in 201 cases with histopathological correlation. Eur Radiol. 2011;21(1):188–96.

93. Bonekamp D, Jacobs MA, El-Khouli R, Stoianovici D, Macura KJ. Advancements in MR imaging of the prostate: from diagnosis to interventions. Radiographics. 2011;31(3):677–703.

94. Vourganti S, Rastinehad A, Yerram NK, Nix J, Volkin D, Hoang A, Turkbey B, Gupta GN, Kruecker J, Linehan WM, Choyke PL, Wood BJ, Pinto PA. Multiparametric magnetic resonance imaging and ultrasound fusion biopsy detect prostate cancer in patients with prior negative transrectal ultrasound biopsies. J Urol. 2012;188(6):2152–7.

95. Kim SH, Park S, Choi SH, Jeong WK, Choi JH. The efficacy of magnetic resonance imaging for the diagnosis of testicular rupture: a prospective preliminary study. J Trauma Acute Care Surg. 2009;66(1):239–42.

96. Fernández-Pérez GC, Tardáguila FM, Velasco M, Rivas C, Dos Santos J, Cambronero J, Trinidad C, San Miguel P. Radiologic findings of segmental testicular infarction. Am J Roentgenol. 2005;184(5):1587–93.

97. Tsili AC, Argyropoulou MI, Giannakis D, Sofikitis N, Tsampoulas K. MRI in the characterization and local staging of testicular neoplasms. Am J Roentgenol. 2010;194(3):682–9.

98. Fedel M, Venz S, Andreessen R, Sudhoff F, Loening SA. The value of magnetic resonance imaging in the diagnosis of suspected penile fracture with atypical clinical findings. J Urol. 1996;155(6): 1924–7.

99. Choi MH, Kim B, Ryu JA, Lee SW, Lee KS. MR imaging of acute penile fracture 1. Radiographics. 2000;20(5):1397–405.

100. Pretorius ES, Siegelman ES, Ramchandani P, Banner MP. MR imaging of the penis 1. Radiographics. 2001;21 Suppl 1:S283–98.

101. Chou CP, Levenson RB, Elsayes KM, Lin YH, Fu TY, Chiu YS, Huang JS, Pan HB. Imaging of female urethral diverticulum: an update. Radiographics. 2008;28(7):1917–30.